Quantifying the Impact of SST Feedback Frequency on the Madden-Julian Oscillation Simulations

Yung-Yao Lan[1], Huang-Hsiung Hsu[1], and Wan-Ling Tseng[2]
[1]Research Center for Environmental Changes, Academia Sinica, Taipei 11529, Taiwan
[2]Ocean Center, National Taiwan University, Taipei 10617, Taiwan
Correspondence to: Huang-Hsiung Hsu (hhhsu@gate.sinica.edu.tw)

Abstract

This study uses the CAM5 coupled to a 1-d ocean model to investigate the effects of intraseasonal SST feedback frequency on the Madden-Julian Oscillation (MJO) simulation with intervals at 30 minutes, 1, 3, 6, 12, 18, 24, and 30 days. The large-scale nature of the MJO in simulations remains intact with decreasing feedback frequency, although becoming increasingly unrealistic in both structure and amplitude, until 1/30days when the intraseasonal fluctuations are overwhelmingly dominated by unorganized small-scale perturbations in both atmosphere and ocean, as well as at the atmosphere-ocean interface where heat and energy are rigorously exchanged. The main conclusion is less frequent the SST feedback, more unrealistic the simulations. Our results suggest that spontaneous atmosphere-ocean interaction with high vertical resolution in the ocean model is the key to the realistic simulation of the MJO and should be properly implemented in climate models.

1. Introduction

The Madden–Julian Oscillation (MJO) is a large-scale tropical circulation that propagates eastward from the tropical Indian Ocean (IO) to the western Pacific (WP) with a periodicity of 30–80 days (Madden and Julian, 1972). In the Indo-Pacific region, the MJO processes involve intraseasonal variability of sea surface temperature (SST) (Chang et al., 2019; DeMott et al., 2014, 2015; Jiang et al., 2015, 2020; Krishnamurti et al., 1998; Li et al., 2014; Li et al., 2020a; Newman et al., 2009; Pei et al., 2018; Stan,

樣式定義: 內文 (Web)
已刪除: To quantify
格式化: 下: 1.5 公分
已刪除: impact
已刪除: feedback periodicity
格式化: 左右對齊
已刪除: atmospheric intraseasonal variability in
已刪除: tropical regions
已刪除: [2]International Degree Program in Climate Change and Sustainable Development
格式化: 左右對齊
已刪除: This study couples a high-resolution 1-D TKE ocean model (the SIT model) with the Community Atmosphere Model 5.3 (CAM5.3; hereafter CAM5–SIT) configuration, to highlight significant experiments that investigate the influence of different periods of sea surface temperature (SST) feedback, such as 30 minutes, 1, 3, 6, 12, 18, and 30 days, on the Madden-Julian Oscillation (MJO). It substantially breaks through the limitations of flux coupler through air–sea coupling. The aim is to assess the scientific reproducibility and consistency of the findings across different SST feedback cycles in the field of modeling science. Comparing the results to the fifth generation ECMWF reanalysis (ERA5), the high-frequency experiments (C–CTL, C–1day, and C–3days) and low-frequency experiments (C–6days, C–12days, and C–18days) exhibit higher fidelity in capturing various aspects of MJO, except for the C–30days experiment. These aspects in characterizing the basic features of the MJO such as encompass intraseasonal periodicity, eastward propagation, coherence in the MJO band, tilting vertical structure, the lead–lag relationship between MJO-related atmosphere and SST variation, phase 2 column-integrated moisture static energy ...
格式化: 左右對齊
已刪除:
格式化: 左右對齊, 縮排: 第一行: 2 字元
已刪除: there is increasing evidence that
已刪除: are involved in

2018; Tseng et al., 2015). The tropical air–sea interaction, influenced by the upper ocean, plays a crucial role in determining MJO characteristics due to the high heat capacity of the upper ocean within the intraseasonal range, which acts as a significant heat source for atmospheric variability (Watterson 2002; Sobel and Gildor 2003; Maloney and Sobel 2004; Sobel et al. 2010; Liang and Du, 2022).

Analyzing the mechanism of the intraseasonal oscillation (ISO) reveals that heat fluxes play a critical role in the development of intraseasonal SST variability (Hong et al., 2017; Liang et al., 2018). As demonstrated in Fu et al. (2017), underestimation (overestimation) of the air–sea coupling's impact on MJO simulations occurs when it is weak (strong) in the intraseasonal SST variability. Simulation improvements in the eastward propagation and regulation of MJO periodicity in the coupled models can be attributed to several factors such as enhanced low-level convergence and convective instability to the east of convection, as well as enhanced latent heat fluxes (Savarin and Chen, 2022) and SST cooling to the west of convection (DeMott et al., 2014). SST gradients have been found to induce patterns of mass convergence and divergence within the marine boundary layer (MBL), initiating atmospheric convection (de Szoeke and Maloney, 2020; Lambaerts et al., 2020).

Several recent studies have made significant progress in understanding the impact of air–sea coupling on the MJO, particularly at sub-daily scales (e.g., DeMott et al., 2015; Kim et al., 2018; Seo et al., 2014; Voldoire et al., 2022; Zhao and Nasuno, 2020). However, there is relatively limited discussion on the effect of air–sea coupling from few days to within half of the MJO period. Several studies have investigated the impact of intraseasonal SST on the MJO by coupled or uncoupled models. (e.g., DeMott et al., 2014; Gao et al., 2020b; Klingaman, and Demott, 2020; Pariyar et al., 2023; Stan, 2018). Simulations using time-varying SSTs from coupled global climate model (CGCM) to force the atmospheric general circulation model (AGCM) showed a reduced

已刪除: These studies confirm that including air–sea interactions significantly improves the simulation of the MJO. The ocean's response to intraseasonal atmospheric variability, such as surface shortwave radiation, turbulent heat fluxes controlled by wind speed, and ocean processes driver ...

已下移 [1]: DeMott et al., 2014; Lan et al., 2022; Stan, 2018; Tseng et al., 2015, 2020).

已刪除: However, the influence of sub-seasonal (e.g., beyond a phase) air–sea coupling on convection and related oceanic ...

已刪除: , which acts as a significant source of heat energy for atmospheric variability (Liang and Du, 2022). The SIT ...

已刪除:

格式化: 內文 (Web), 左右對齊, 縮排: 第一行: 2 字元, 格線被設定時，自動調整右側縮排, 調整中文/英文字之間的空白, 調整中文/數字之間的空白

已下移 [2]: Several recent studies have made significant progress in understanding the impact of air–sea coupling on

已刪除: However, there is relatively limited discussion on air–sea coupling at the sub-seasonal scale. Several studies ...

已下移 [3]: (e.g., DeMott et al., 2014; Gao et al., 2020b; Klingaman, and Demott, 2020; Pariyar et al., 2023; Stan,

已刪除: Stan (2018) found that in the air–sea coupling run, the peak in surface fluxes (latent heat and sensible heat) is ...

已下移 [4]: , leading to weakened air–sea heat fluxes and eastward propagation (DeMott et al., 2014; Gao et al., 2020b;

已刪除: Stan (2018) also demonstrated that eliminating 1–5-day variability of surface boundary forcing reduces the ...

已刪除: there is weakness (strong) in the intraseasonal SST anomaly. Understanding the manifestation of heat fluxes in ...

已刪除: , contribute to the improved eastward propagation and regulation of MJO periodicity

已刪除: The basic state SST or basic state moist static energy (MSE) plays a crucial role in MJO instability (Wang ...

已移動 (插入) [2]

已移動 (插入) [3]

intraseasonal SST variability, leading to weakened air–sea heat fluxes and eastward propagation (DeMott et al., 2014; Gao et al., 2020b; Klingaman, and Demott, 2020; Pariyar et al., 2023). Moreover, the absence of few days variability in SST promotes the amplification of westward power associated with Rossby waves (Stan, 2018).

Incorporating two-way coupling between the ocean and atmosphere has been proved valuable for simulating and predicting intraseasonal variability (e.g., DeMott et al., 2014; Lan et al., 2022; Stan, 2018; Tseng et al., 2015, 2020). As demonstrated in recent studies (e.g., Ge et al. 2017, Lan et al., 2022, Shinoda et al. 2021, and Tseng et al. 2015, 2022), incorporating high vertical resolution near the ocean surface positively influences the accurate representation of intraseasonal SST variability and enhances the MJO prediction capabilities. However, how frequent is the coupling needed is still not fully understood, considering the fact that the ocean and atmosphere could evolve in distinct time scales. And, would the coupling frequency in numerical models influence the accuracy of the MJO simulation?

In this study, we aim to investigate the specific effects of oceanic feedback frequency (FF) through air–sea coupling on the atmospheric intraseasonal variability, using the National Center for Atmospheric Research (NCAR) Community Atmosphere Model 5.3 (CAM5.3) coupled with the single-column ocean model named Snow–Ice–Thermocline (SIT). The coupled model is referred to as CAM5–SIT. The SIT model, consisting of 41 vertical layers, enables the simulation of SST and upper-ocean temperature variations with high vertical resolution (Lan et al., 2022). We have demonstrated in previous studies that coupling the SIT significantly improved the MJO simulations in several AGCMs (Tseng et al. 2015, 2022, Lan et al. 2022). The ability of the SIT with extremely high-resolutions (i.e., 12 layers within the first 10.5 m) to well resolve the upper ocean warm layer and the cool skin of the ocean surface was identified as the main reason for the improved simulations.

已移動 (插入) [4]

已移動 (插入) [1]

已移動 (插入) [5]

已移動 (插入) [6]

已刪除:

The structure of this paper is organized as follows. Section 2 introduces the model, data, methodology, and experiments employed in this study. The performance of the CAM5–SIT models in simulating the MJO is discussed in Section 3, while Section 4 focuses on the impact of different configurations of sub-seasonal SST feedback periodicity on MJO simulations. Finally, Section 5 presents the conclusions.

2. Data, model experiments, and methodology

2.1 Observational data

Observational data sets used in this study include precipitation from the Global Precipitation Climatology Project (GPCP, 1° resolution, 1997–2010; Adler et al., 2003), outgoing longwave radiation (OLR, 1° resolution, 1997–2010; Liebmann, 1996), and daily SST (optimum interpolated SST, OISST, 0.25° resolution, 1989–2010; Banzon et al., 2014) from the National Oceanic and Atmosphere Administration, and the fifth generation ECMWF reanalysis (ERA5), with a resolution of 0.25° for the period of 1989–2020 (Hersbach and Dee, 2016). Various variables from ERA5 were considered, including winds, vertical velocity, temperature, specific humidity, sea level pressure, geopotential height, latent and sensible heat, and shortwave and longwave radiation. For the initial conditions of the SIT, the SST data was obtained from the Hadley Centre Sea Ice and Sea Surface Temperature dataset version 1 (HadISST1), with a resolution of 1° for the period of 1982–2001 (Rayner et al., 2003). The ocean subsurface data, including climatological ocean temperature, salinity, and currents in 40 layers, were retrieved from the National Centers for Environmental Prediction (NCEP) Global Ocean Data Assimilation System (GODAS) with a resolution of 0.5° for the period of 1980–2012 (Behringer and Xue, 2004). These data were used for a weak nudging (Tseng et al. 2015 2022; Lan et al. 2022) in the SIT model.

已刪除: models

格式化: 左右對齊

已刪除: methodologies

已刪除: configurations

已刪除: through detailed MJO diagnostics.

已刪除: drawn from this study.

已刪除: **, atmospheric, and oceanic**

已刪除: An observational

已刪除: set

已刪除: includes

已刪除: .
The atmospheric variables used in this study were obtained from the fifth-generation reanalysis of the European Centre for Medium-Range Weather Forecasts (ECMWF) known as

已刪除: zonal wind, meridional wind

已刪除: heat,

已刪除: a

已刪除: model,

2.2 Experimental design

In this study, we investigated the role of oceanic FF using coupled CAM5–SIT and atmosphere-only CAM5 (A–CTL). Previous studies (Lan et al., 2022; Tseng et al., 2022) have provided a detailed description of the every timestep coupling CAM5–SIT model and its performance in simulating the MJO. Table 1 displays the experimental configuration, incorporating monthly HadISST1 (uncoupled region) and ice concentrations over a 30-year period centered around the year 2000 (F2000 compsets, Rasch et al., 2019). Solar insolation, greenhouse gas and ozone concentrations, and aerosol emissions representative of present-day conditions were prescribed. In the A–CTL, observed monthly-mean SST around the year 2000 was prescribed to force the CAM5. For the coupled simulations, we adjusted the Flux Coupler (CPL) restriction in the Climate Earth System Model (CESM1; Hurrell et al., 2013) by implementing asymmetric exchange frequencies between the atmosphere and the ocean. The ocean continuously receives atmospheric forcing at every time step (30 minutes) and the temperature changes accordingly, but the SST seen by the atmospheric model is fixed at each timestep for a specified time span (e.g., 1, 3, 6, 12, 18, 24, and 30 days). That is, the SST seen by the atmospheric model only changed until the end of the specified time span.

Two sets of experiments in addition to the A–CTL were conducted, each representing a different SST feedback frequency:

(1) High-frequency SST feedback set: This set includes the control experiment (C–CTL) with SST feedback at every timestep (FF as 48/day), once a day (C–1day: FF as 1/day), and every 3 days (C–3days: FF as 1/3days).

(2) Low-frequency SST feedback set: This set includes experiments with SST feedback to the atmosphere for every 6 days (C–6days: FF as 1/6days), 12 days (C–12days: FF as 1/12days), 18 days (C–18days: FF as 1/18days), 24 days (C–

已刪除: investigate
已刪除: in sub-seasonal periodicity
已刪除: the
已刪除: model
已刪除: the uncoupled AGCM
已刪除: atmospheric variability
已刪除: the MJO. This study involved
已設定格式: 字型色彩: 自動
已刪除: series of
已移動 (插入) [7]
已設定格式: 字型色彩: 自動
已刪除: numerical experiments (as shown in Table 1). We overcame
已刪除: limitations of the National Center for Atmospheric Research (NCAR)
已刪除: CSM) Flux Coupler (CPL)
已刪除: similarly
已刪除: The SST value
已刪除: within the experimental periodicity through
已刪除: straightforward approach to create various intraseasonal SST
已刪除: 30 minutes,
已刪除:) feedback atmospheric experiments. It is important to note that every timestep involves bidirectional interaction in the CPL.
已刪除: The high
已刪除: as well as experiments with SST feedback
已刪除:)
已刪除:), respectively.
已刪除: The low
已刪除: returning

24days: FF as 1/24days), and 30 days (C–30days: FF as 1/30days).

The SIT is coupled to CAM5 between 30° N to 30° S. The ocean was weakly nudged (using a 30-day exponential time scale) between depths of 10.5 m and 107.8 m, and strongly nudged (using a 1-day exponential time scale) below 107.8 m, based on the climatological ocean temperature data from NCEP GODAS. No nudging was applied in the upper-most 10.5 meters, allowing the simulation of rigorous air–sea coupling near the ocean surface.

During the simulation, the SIT recalculated the SST within the tropical air–sea coupling region. Outside this coupling region, the annual cycle of HadSST1 was prescribed. No SST transition between the tropical air–sea coupling zone and the extratropical SST-prescribed regions was applied. The ocean bathymetry for the SIT was derived from the NOAA's 1 arc-minute global relief model of Earth's surface that integrated land topography and ocean bathymetry (ETOPO1) data (Amante and Eakins, 2009). To ensure consistency and comparability, all observational, atmospheric, oceanic, and reanalysis data were interpolated into a horizontal resolution of 1.9° × 2.5° for model initialization, nudging, and comparison of experimental simulations.

2.3 Methodology

The analysis focused on the boreal winter period (November–April), the season with the most pronounced eastward propagation of the MJO. To identify intraseasonal variability, the CLIVAR MJO Working Group diagnostics package (CLIVAR, 2009) and a 20–100-day filter (Wang et al., 2014) was used. MJO phases were defined based on the Real-time Multivariate MJO series 1 (RMM1) and series 2 (RMM2) proposed by Wheeler and Hendon (2004), which utilized the first two principal components of combined near-equatorial OLR and zonal winds at 850 and 200 hPa. The band-pass filtered data were used to calculate the index and define the MJO phases.

已刪除:), respectively.

已刪除: In all experiments, there

已刪除: a common configuration:

已刪除: forces SIT at each timestep, SIT has the same vertical resolution, and coupling is implemented

已刪除: in the entire tropics. The only difference lies in the frequency of SIT's SST feedback into the atmosphere. This choice is driven by two factors related to tropical coupling. Firstly, the MJO predominantly occurs in tropical regions (Jiang et al., 2020; Kang et al., 2020; Shinoda et al., 2021), hence coupling was specifically implemented between 30° N to 30° S. This focuses the coupling on the region where the MJO is most active.
Secondly, coupling a one-dimensional ocean model without surface flux correction to the extratropics would neglect the influence of strong ocean currents, such as the Kuroshio and Gulf Streams, leading to significant biases. Therefore, coupling is limited to the tropical region to avoid these biases and ensure a more realistic representation of the air–sea interactions relevant to the MJO.
Forcing of the coupled and uncoupled models' initial ...

已刪除: .

已刪除: , which spans from 30° S to 30° N.

已刪除: prescribed

已刪除: used.

已設定格式: 字型色彩: 自動

已刪除:

已刪除: primarily

已刪除: which exhibits

已刪除: were employed.

已刪除: following

已刪除: index (namely,

已刪除: utilizes

已刪除: employed

Analysis of column-integrated MSE budgets was conducted to investigate the association between tropical convection and large-scale circulations. The column-integrated MSE budget equation (e.g., Sobel et al., 2014) is approximately given by

$$\langle \frac{\partial h}{\partial t} \rangle' = -\langle u\frac{\partial h}{\partial x}\rangle' - \langle v\frac{\partial h}{\partial y}\rangle' - \langle w\frac{\partial h}{\partial p}\rangle' + \langle LW\rangle' + \langle SW\rangle' + \langle SH\rangle' + \langle LH\rangle' \qquad (1)$$

where h denotes the moist static energy

$$h = c_p T + gz + L_v q \qquad (2)$$

where T is temperature (K); q is specific humidity (Kg Kg^{-1}); c_p is dry air heat capacity at constant pressure (1004 J K^{-1} kg^{-1}); L_v is latent heat of condensation (taken constant at 2.5×10^6 J kg^{-1}); u and v are horizontal and meridional wind (m s^{-1}), respectively; ω is the vertical pressure velocity (Pa s^{-1}); LW and SW are the longwave and shortwave radiation flux (W m^{-2}), respectively; and LH and SH are the latent and sensible surface heat flux (W m^{-2}), respectively. The angle bracket ($\langle * \rangle$) represents mass-weighted vertical integration from 1000 to 100 hPa; and the intraseasonal anomalies are represented as $\langle * \rangle'$.

3. Results

3.1 The mean state and intraseasonal variability of SST

The variability of SSTs plays a crucial role in the dynamics of the MJO. Studies based on observations from TOGA COARE and DYNAMO revealed that MJO events exhibited a stronger ocean temperature response compared to average conditions (de Szoeke et al., 2014). Wu et al. (2021) revealed the better MJO prediction skill in the CGCM could be contributed by the improved representation of high-frequency SST fluctuations related to the MJO, with warm (cold) SST anomalies to the east (west) of MJO convection, through the convection–SST feedback processes (Li et al., 2020a; Wu et al., 2021). It is therefore necessary to check on the influences of coupling and coupling frequency on the SST fluctuations.

已刪除: Furthermore, an analysis

已刪除: the

已刪除: ;

已刪除: velocities

已刪除: fluxes

已刪除: fluxes

已刪除: brackets ($\langle * \rangle$) represent

已刪除: $\langle * \rangle'$, which were isolated using a 20–100-day bandpass filter (Wang et al., 2014).

格式化: 左右對齊, 縮排: 第一行: 0 公分

格式化: 左右對齊

已刪除: **basic**

已刪除: **variability**

已刪除: In the absence of interseasonal SST variability, as observed in the uncoupled A–CTL simulations, the eastward propagation of the MJO is disrupted, resulting in weakened or fragmented MJO activity.

已刪除: have

已刪除: exhibit

已刪除: Interseasonal

已刪除: variability in the tropics, resulting from air–sea coupling, significantly impacts the behavior of the MJO behavior and atmospheric circulation. Warmer SSTs

已刪除: enhance

已刪除: release of latent heat, triggering atmospheric

已刪除: strengthening the MJO. Conversely, cooler SSTs in this region create a more stable atmospheric environment, which is less favorable for the development and propagation of the MJO (DeMott et al., 2015). The activity and strength of the MJO are influenced by SST in the region. Cooler than average sea surface temperatures (SSTs) in this region are associated with the passage of MJO activity and a tendency towards decreased intensity. …

Table 2 presents the oceanic temperature anomalies for the DJF seasonal mean, including the differences in oceanic temperature between the SST and depths of 10m ($\Delta \boldsymbol{T}_{\mathbf{0-10}\boldsymbol{m}}$) and 30m ($\Delta \boldsymbol{T}_{\mathbf{0-30}\boldsymbol{m}}$), as well as 20–100 days maximum and minimum SST and oceanic temperature at 10m depth (T_{10m}). The region of 110–130° E and 5–15° S was selected because of the largest variation in the 20–100-day bandpass-filtered SST when the MJO passes over the Indo-Pacific region. Simulated DJF seasonal mean SST (300.8K to 302.0 K) are generally smaller than OISST (302.2 K) but increase with the lower SST feedback frequency except in C–30days (302.7 K), while the SST standard deviation remains within 0.8 K, smaller than OISST (0.96 K), except in C–24days (1.06 K) and C–30days (1.71 K).

The simulated subsurface (0–10m and 0–30m) ocean temperatures were compared with those in the NCEP GODAS reanalysis and presented as ($\Delta \boldsymbol{T}_{\mathbf{0-10}\boldsymbol{m}}$ and $\Delta \boldsymbol{T}_{\mathbf{0-30}\boldsymbol{m}}$). The $\Delta \boldsymbol{T}_{\mathbf{0-10}\boldsymbol{m}}$ in high-frequency experiments maintained 0.1 K temperature difference. In low-frequency experiments, $\Delta \boldsymbol{T}_{\mathbf{0-10}\boldsymbol{m}}$ increased from 0.2 to 1.0 K with decreasing SST feedback frequency. The temperature difference ($\Delta \boldsymbol{T}_{\mathbf{0-30}\boldsymbol{m}}$) in both high-frequency and low-frequency experiments remains approximately 0.8K, except for C–24days and C–30days with an increase as high as 1.4 K and 2.1 K, respectively. The comparison revealed the cooling effect of the SIT on the seasonal mean SST, especially in the higher-frequency coupling experiment due to the more rigorous heat exchanges between ocean and atmosphere. However, in the lower frequency experiments, the SST became much warmer and so did vertical temperature differences due likely to the unrealistically large heat accumulation of loss in the ocean.

As for the MJO simulation, the SST fluctuation is more relevant. The OISST fluctuation through a MJO cycle was about ±0.21 K. In comparison, the uncoupled A–CTL, which was forced by monthly mean HadISST1, yielded a negligible SST fluctuation (-0.003–0.02 K) as expected. In the high-frequency experiments, SST

已刪除: phase anomalies of

已刪除: it shows

已刪除: Except for C–30days, the

已刪除: shows a slight

已刪除: higher

已刪除: periodicity,

已刪除: . In the critical region (110–130° E, 5–15° S), experiments with high frequency SST feedback periodicity exhibit a mean SST of less than

已刪除: 4 K during DJF, while experiments with low frequency SST feedback periodicity range from -

已刪除: 0 K to 0.5 K compared to the OISST dataset.

已刪除: Understanding the variations in SST during DJF in the Indo-Pacific region is critical for predicting

已刪除: interpreting the MJO's behavior. The temperature differences between observed monthly mean SST and

已刪除: data

已刪除:) as well as AGCM are not compared here.

已刪除: maintain

已刪除: 1K

已刪除: $\Delta \boldsymbol{T}_{\mathbf{0-10}\boldsymbol{m}}$ increase

已刪除: 1

已刪除: as

已刪除: periodicity increases correspondingly.

已刪除: 30days. In the daily OISST SST phase anomalies, the maximum

已刪除: minimum values are approximately maintained at ±0.2K. However, compared to OISST or model simulations, the uncoupled A–CTL, which uses monthly mean OISST, ...

已刪除: –2 magnitudes smaller.

格式化: 左右對齊, 縮排: 第一行: 2 字元

fluctuated in magnitudes similar to that in the daily OISST. The amplitude became unrealistically larger in the low-frequency coupling experiments with C–30days reaching as high as 0.6 K. The increasingly larger amplitudes were likely resulted from the heat accumulation in the ocean because of less frequent feedback (or heat release) to the model atmosphere. Changes in coupling frequency led to different amplitudes of SST fluctuation in a MJO cycle. As will be revealed latter, this effect had marked influence on the MJO simulations.

3.2 MJO simulation: high-frequency and low-frequency SST feedback experiments

3.2.1 General structure

The propagation characteristics of the different experiments were analyzed using the wavenumber-frequency spectrum (W-FS). The spectra of unfiltered U850 in ERA5, A–CTL, and all coupling experiments with different feedback frequency are shown in Fig. 1a–i. The C–CTL experiment accurately captures the eastward propagating signals at zone wavenumber 1 with 30–80-day period (Fig. 1a and 1c), although with a slightly larger amplitude than ERA5 (Fig. 1a). By contrast, the uncoupled A–CTL produced an unrealistic spectral shift to time scales longer than 30–80 days (Fig. 1b) and simulated the unrealistic westward propagation at wavenumber 2.

The W-FS spectra of the C–1day and C–3day experiment show two peaks for zone wavenumber 1 over the 30 to 80-day period. The low-frequency experiments (i.e., from C–6days to C–30days) increasingly enhanced the amplitudes and lowered the frequency of intraseasonal perturbations with decreasing feedback frequency. Furthermore, unrealistic westward W-FS of U850 becomes evident in (Fig. 1h–i) in the C–18days, C–24days, and C–30days experiments, reflecting the stationary nature of simulated MJO.

已刪除: phase anomalies exhibit

已刪除: magnitudes of ±0.2K as observed. The SST means in both the high-frequency and low-frequency experiments reach their maximum in phase 3, lagging about 1 phase behind the OISST. The maximum and minimum T_{10m} values indicate

已刪除: the atmospheric heat/cooling ocean process is consistently mixed

已刪除: C–CTL experiment, but not

已刪除: According to CLIVAR diagnostics, there are diverse behaviors observed in MJO simulations, as indicated by the slight difference between phase anomalies of C–3days maximum SST and T_{10m} compared to C–CTL and C–1day, which indicates diverse behaviors of MJO simulations, according to CLIVAR diagnostics. Fu et al. (2017) indicated that too weak intraseasonal SST anomaly in coupled models would lead to the underestimation of the impacts of air–sea coupling on MJO simulations.

格式化: 左右對齊

已刪除: We conducted SST feedback experiments with ...

已刪除: reanalysis

已刪除: C–CTL, C–1day, C–3days, C–6days, C–12days, C ...

已刪除: C–30days

已刪除: i, respectively.

已刪除: and for periods of

已刪除: to

已刪除: days

已刪除: . However

已刪除: produces

已刪除: exhibits

已刪除:

已刪除: C–3days tend to reduce the interseasonal ...

The Hovmöller diagrams in Fig. 2a–i depict the evolution of 10° N–10° S averaged precipitation and U850 anomalies on intraseasonal timescales, represented by the lagged correlation coefficients with the precipitation averaged over 10° S–5° N, 75–100° E. In GPCP/ERA5, observed precipitation and U850 propagated eastward from the eastern IO to the dateline, with precipitation leading U850 by approximately a quarter of a cycle, and a propagation speed of about 5 m s^{-1} (Fig. 2a). The A–CTL simulation was dominated by stationary features, with westward-propagating tendency over the IO and weak and slow eastward propagation over the MC and WP (Fig. 2b). The Hovmöller diagrams derived from high-frequency and low-frequency experiments (Fig. 2c–h) display the key eastward propagation characteristics in both precipitation and U850, as well as the phase relationship between them, except in C–24days and C–30days that were dominated by stationary perturbations. Further decreased feedback frequency from 1/C–24days to 1/C–30days also further weakened the signals of precipitation and U850. More detailed discussion on this topic will be presented in the subsequent chapter.

We conducted a wavenumber-frequency power spectral analysis (Wheeler and Kiladis 1999) to examine the phase lag and coherence between the tropical circulation and convection. Figures 3a–i illustrate the symmetric part of OLR and U850 for NOAA/ERA5 data and all model experiments. The MJO band exhibits a high degree of coherence, indicating a strong correlation between NOAA MJO-related OLR signal and wavenumbers 1–3 (Fig. 3a). The phase lag in the 30–80-day band is approximately 90°, consistent with previous studies (Ren et al., 2019; Wheeler and Kiladis 1999). All model experiments simulated the coherence within wavenumber 3 in the MJO band, with a phase lag similar to NOAA/ERA5 data. However, the A–CTL spectrum exhibits only half of the observed coherence peak at wavenumber 1, and also weaker coherence at wavenumbers 2–3 for the 30–80-day period compared to NOAA/ERA5 data. The

已删除: 1day experiment showed two peaks for zone wavenumber 1 over the 30 to 80-day period. This might be attributed to the inconsistency in day and night variations when the SST feedback of C–1day is returned to the atmosphere at different locations. Except for C–30days, the low-frequency experiments enhance the W-FS of U850 during interseasonal periods. In this study, low-frequency SST variability is not enhanced in the unrealistic westward W-FS by increasing SST feedback periodicity until C–18days.

已删除: i

已删除: between

已删除: there is

已删除: eastward propagation of

已删除: . The

已删除: the 30–80-day filtered U850 anomaly is

已删除: However, the

已删除: simulations exhibit

已删除: signals

已删除: ,

已删除: 2b), which is also reflected in the W-FS shown in Fig. 1b, indicating enhanced westward propagation in ...

已删除: of the

已删除: of both precipitation and U850, as well as the phas ...

已删除: cross-

已删除: , A–CTL, C–1day, C–3days, C–6days, C–12days, C ...

已删除: simulated

已删除: show significant

已删除: at wavenumber 1 only

已删除: coherency peaks

已删除: the

已删除: is weaker

experiments C–CTL, C–1day, C–3days, C–6days, C–12days, and C–18days yielded wavenumber-1 coherence peak similar to that in NOAA/ERA5. Additionally, as the SST feedback frequency decreases from 1/12days to 1/30days, the experiments increasingly simulated unrealistic coherence in the very low frequency with a wide range of zonal wavenumber from 1 to 12 (Fig. 3g–j), i.e., no zonal scale preference.

Figure 4 shows the phase–longitude diagrams in which the 20–100-day filtered precipitation (shaded) and SST (contour) anomalies were averaged over 10° S to 10° N to determine the relationship between precipitation and SST fluctuations and to provide insights into the connection between air–sea coupling and convection. As expected, the A–CTL did not simulate the eastward-propagating coupled SST-convection perturbations as in observation (Fig. 4a), whereas C–CTL, C–1day, and C–3days properly reproduced the observed features. The eastward-propagating coupled perturbations were also simulated in C–6days, C–12days, and C–18days, but with unrealistically increasing amplitudes near the dateline, especially in the C–18days experiment. The perturbation amplification near the dateline was likely due to the lack of ocean circulation in the CAM5–SIT. The amplification was also seen in C–24days that failed to simulate the eastward-propagating intraseasonal perturbations. When coupling frequency was reduced to 1/30days, the eastward propagation could no longer be simulated and was replaced by unorganized standing oscillations in much smaller zonal scales.

Liang et al. (2018) suggested that SST leading precipitation by 10 days implies air–sea interactions at the intraseasonal timescale during MJO events, with SST playing a crucial role in modulating the MJO's intensity and propagation. The A–CTL simulation exhibited weak SST anomalies and stationary precipitation when using the monthly average HadISST1. By contrast, the C–24days and C–30days experiment showed no clear phase lag between SST and precipitation perturbations. A comparison

已刪除: exhibit

已刪除: coherency peaks

已刪除: at wavenumber 1.

已刪除: periodicity increases

已刪除: between C–12days and C–30days simulate

已刪除: coherency over

已刪除: 9 in the MJO band

已刪除:).

已刪除: The

已刪除: anomalies

已刪除: anomalies

已刪除: the

已刪除: –

已刪除: region (Fig. 4a–i). Phase-longitude diagrams were used to analyze

已刪除: establish

已刪除: Except for C–30days, both GPCP/OISST and the coupled experiments clearly showed

已刪除: propagation of enhanced

已刪除: with positive SST anomalies (Fig. 4a and 4c–i). The amplitude of SST increases in low-frequency experiments,

已刪除: indicated

已刪除: Table 1 and Fig. 4f–h, resulting in precipitation anomalies lagging by approximately 2–3 phases than SST, particularly when crossing the MC. Liang et al. (2018) indicated

格式化: 左右對齊, 縮排: 第一行: 2 字元

已刪除: simulations

已刪除: SST interpolation from OISST. In

已刪除: unrealistic SST and precipitation variability. Overall, eastward propagation of the MJO is not favored by either minimal or large SST fluctuations between simulation results and observation indicates that the air–sea interaction plays a crucial role in facilitating eastward propagation and higher frequency feedback yields more realistic simulations.

3.2.2 Vertical structures of the MJO in the atmosphere

Air–sea interaction plays a significant role in influencing atmospheric moisture and convection associated with the MJO (Savarin and Chen, 2022). Whereas the ocean to the east of deep convection warmed due to more downwelling shortwave radiation and less heat fluxes into the atmosphere associated with weaker winds, near-surface moisture convergence under the anomalous subsidence over the warmer water preconditioned the eastward movement of the deep convection (DeMott et al., 2015; Zhang, 2005). The MJO was noted to detour southward when crossing the MC region, exhibiting enhanced convective activity preferentially in the southern MC area and weaker convection in the central MC area (Hsu and Lee 2005, Wu and Hsu 2009, and Kim et al. 2017). Hovmöller diagrams in Fig. 5a–j illustrate the relationship between the vertical structure of air temperature (contoured, in K) and specific humidity (shading, in g kg^{-1}) anomalies from the surface to 200 hPa averaged over 5–20° S and 120–150° E. In ERA5, the lower-level positive temperature anomaly in phase 3 (i.e., preconditioning phase) leads the development of deep temperature and moisture anomalies (i.e., deep convection) after phase 4 over the MC, when moisture anomalies reached the maxima at 700–500 hPa. This two-phase upward development was not properly simulated in A–CTL, which shows sudden switch between positive and negative anomalies in the entire troposphere, instead of progressively upward development with time. The upward development was generally simulated in coupled simulations from C–CTL to C–6days (Fig. 5c–e), although the negative temperature anomalies below 500 hPa were over-simulated after phase 5. It became less well

- 已下移 [8]: (Fig.
- 已設定格式: 字型色彩: 自動
- 已刪除: 4b and 4i). By comparing the coupled experiments with the aforementioned simulations, it became evident that
- 已刪除: . Fu et al. (2017) found that a robust intraseasonal SST anomaly is associated with successive MJO events and supports the propagation of MJOs, as supported by NOAA OLR and TRMM precipitation. This study highlights the significant improvement in eastward propagation simulation ...
- 已刪除: and low-frequency experiments, even with a simpl ...
- 格式化: 左右對齊
- 已刪除: During periods of convective suppression,
- 已刪除: air temperature generally tracks the SST closely (d ...
- 已刪除: , leading to increased low-level moisture and ...
- 已刪除: propagation and
- 已刪除: 2014).
- 已刪除: i
- 已刪除: anomalies
- 已刪除: the vertically tilting structure of
- 已刪除: the upper troposphere (
- 已刪除:)
- 已刪除: the 10
- 已刪除: –10° N
- 已刪除: regions. Positive air
- 已刪除: lead positive specific humidity
- 已刪除: by approximately 2–3 phases, with the maximum ...
- 已刪除: In ERA5 and the
- 已刪除: experiments (excluding
- 已刪除: 30days), there are two relatively high values of air ...
- 已刪除: 5b). A–CTL also exhibits a decrease in low-level ...
- 已刪除: 700 hPa. C–30days, on the other hand, shows an ...

simulated beyond C–12days and was gradually replaced by sudden phase switch as in the A-CTL, especially in C–30days (Fig. 5f–j). The preconditioning phase completely disappears in C–18 days and beyond. As identified in previous studies, the two-phase upward development is a manifestation of air–sea coupling. The missing of this coupling evidently resulted in the poor simulation in the A-CTL and extremely low feedback frequency experiments.

3.2.3 Vertical structures of the MJO in the ocean

The 1-D turbulence kinetic energy (TKE) ocean model incorporates a high vertical resolution that captures the vertical gradient of temperature in the upper ocean. Figure 6 (left column) illustrates the vertical structures of oceanic temperature between 0- and 60-meters during phase 2–3 when the deep convection occurred over the eastern IO (60–90° E) and easterly anomalies prevailed over the MC and western Pacific. In the high-frequency experiments (Fig. 6a, 6c, 6e), the upper oceanic temperatures exhibit warming patterns within 30 meters depth at 100–140° E (i.e., east of the deep convection and under the easterly anomalies), apparently due to more downwelling short wave radiation and less heat flux release to the atmosphere. By contrast, the cooling near the dateline was associated with westerly anomalies. With decreasing feedback frequency, the cooling to the east of 150°E seen in high frequency experiments was replaced by oceanic warming that amplified with further feedback frequency decrease. The warming region that became more widespread and larger amplitude with less frequent feedback eventually grew to cover the entire IO and WP, an area much larger than the scale of the atmospheric MJO. The mismatch between the atmospheric and oceanic anomalies suggested the weakening atmospheric-ocean coupling that resulted in poor simulation of the MJO in the low frequency feedback simulations. The emergence of small-scale unorganized structures with decreasing feedback frequency

已删除: destabilization of the MJO. East of the convective MJO, enhanced easterly winds induce atmospheric destabilization and moistening, leading to the propagation of the MJO (Sentić et al., 2020). Figure 6 displays the averaged p-vertical velocity anomaly (OMEGA, Pa s^{-1}, shaded) and zonal wind anomaly (m s^{-1}, contour, interval 0.5) between phase 3 and phase 4 over the 15° N–15° S region. We specifically selected the phase between 3 and 4 to examine the period leading up to the MJO convection crossing the MC. Prior to the onset of the MJO in this phase, there is typically a buildup of convection over the land areas of the MC, which encompass countries such as Indonesia, Malaysia, and the Philippines. This land convection acts as a precursor to the MJO as it creates favorable conditions and sets the stage for the subsequent development of organized atmospheric disturbances. This can be observed in the low-level ascending OMEGA shown in Figure 6a, specifically between 120–150° E. The land convection over the MC is driven by a combination of factors, including the local geography, land-ocean temperature contrasts, and large-scale atmospheric conditions. The complex topography and the presence of extensive water bodies surrounding the MC provide favorable conditions for the uplift of moist air, which leads to the formation of local convection. Additionally, the temperature differences between the warm ocean waters and the relatively cooler land surfaces contribute to the instability and uplift of air masses.

已删除: In C–CTL, there is an enhanced easterly wind anomaly between 120° E and 180° E at 800–600 hPa (Fig. 6c). The stronger easterly winds, coupled with radiative heating, such as net downwelling surface solar radiation, lead to warmer upper ocean temperatures (not shown). This heat stored in the upper ocean influences surface fluxes and drives convection in the atmosphere (de Szoeke et al., 2014; Hsu is also evident in phase 4-5 (right column of Fig. 6), e.g., negative ocean temperature anomalies in the Indian Ocean under the prevailing westerly anomalies.

4. Discussion

4.1 Dynamic lead–lag relationship in intraseasonal variability

The lead–lag relationship refers to a situation where one variable (leading) is cross-correlated with the values of another variable (lagging) in subsequent phases, particularly in the case of SST fluctuations and MJO-related atmospheric variations between phase 1 and 8 within the domain of 110–130° E and 5–15° S (Fig. 7). The analyzed variables include 20–100-day filtered latent heat flux (LHF, indicated by green shading), OLR (indicated by a yellow bar chart), net surface solar radiation (FSNS, indicated by an orange bar chart), U850 (indicated by a purple bar chart), 30-meter depth oceanic temperature (30-m T multiplied by 100, indicated by a black line), and SST (multiplied by 10, indicated by an orange line). Positive value in LHF and FSNS represents an upward flux from ocean to atmosphere.

Decrease in LHF, which indicates a reduction in heat loss from the ocean, and negative FSNS, indicating that solar radiation is heating the ocean, coincide with easterly anomaly that contributes to positive SST anomaly in ERA5 (Fig. 7a). Reversed fluxes are associated with westerly anomalies. This lead–lag relationship depicts the in-situ atmospheric forcing on the oceanic variability during a MJO. As the MJO convection progresses through the region (110–130° E and 5–15° S), several changes in atmospheric and oceanic variables occur. These changes include a shift in OLR from positive to negative values, a decrease in SST, a transition to westerly winds, and an increase in positive FSNS and LHF (Fig. 7a). The temporal variations in SST anomaly from C–CTL to C–12days were predominantly influenced by FSNS, with LHF playing a secondary role, similar to the findings of Gao et al. (2020a). With the exception of

已上移 [7]: et al., 2019).

已上移 [5]: Lan et al., 2022).

已設定格式: 字型色彩: 自動

已刪除: In the western IO and MC region (Fig. 6c–h), there is a spatial distribution of negative OMEGA (ascending motion) anomalies during phase 3–4, accompanied by westerly wind anomalies to the west of MJO convection below 500 hPa in the coupled experiments (except C–30days). In A–CTL during phase 3–4, negative OMEGA anomalies are observed both east and unrealistically west of the MC (Fig. 6b). Generally, the low-frequency experiments exhibit stronger negative OMEGA, westerly wind anomalies and land convection compared to the high-frequency experiments, except for C–30days. In the case of C–30days, deep convection in the IO, MC, and WP regions is weakened as local convection occurs randomly during phase 3–4 (Fig. 6i).

The vertical structure of the ocean responds to the MJO ...

已刪除: These oceanic changes, in turn, induce atmospheric ...

已設定格式: 圖樣:清除

已刪除: **Empirical Orthogonal Function (EOF) analysis** ...

已刪除: **of**

已刪除: 9

已刪除: consist of

已刪除:) which positive values are represented by an upward ...

已刪除: The decrease

已刪除: the

已刪除: zonal winds

已刪除: contribute

已刪除: 9a).

已刪除: changes in LHF, FSNS, OLR, U850 and SST which ...

已刪除: circulation patterns

已刪除: 9a).

experiments of A–CTL, C–24days, and C–30days, both the high-frequency and low-frequency SST feedback experiments simulated similar lead–lag relationships as in ERA5 (Fig. 7c–h). In the C–24days and C–30days experiments, LHF was the largest flux term (note the different vertical scale for the two experiments) whereas the wind, OLR, and FSNS anomalies were much weaker than in other experiments. In the A–CTL experiment, which was forced by monthly HasISST1 data, the SST anomalies were small as expected, whereas fluxes although weak are still evident in response to atmospheric perturbations (Fig. 7b). Conversely, in both C–24days and C–30days experiments, a misalignment in the lead–lag relationship was observed, accompanied by weak anomalies in OLR and FSNS. (Fig. 7i and 7j). This disparity between LHF and wind was likely due to the unrealistically widespread and large oceanic warming as shown in Fig. 6m and 6o.

In the simulations, the maximum positive anomaly in 30-m T was delayed by one phase compared to SST, indicating the transfer of heat from the ocean surface into the upper ocean progressively. Similarly, the occurrence of the most negative 30-m T anomaly was also delayed by one phase compared to SST, revealing the buffering role of the upper ocean when the atmospheric component of the MJO extracted (or deposited) heat (energy) from (in) the ocean (Fig. 7c–i). This delayed effect was also evident in the field campaign. de Szoeke et al. (2015) observed that the warmest 10-m ocean temperature occurred a few days later than the peak temperature at 0.1 m. Additionally, the 0.1-m ocean temperature was typically as warm as or warmer than the 10-m temperature as seen in Fig. 6. In the extreme low frequency feedback experiments, the amplitude of 30-m temperature became unrealistically large due likely to the continuous accumulation or loss of the ocean heat.

4.2 Unorganized perturbations in extreme frequency feedback scenarios

已刪除: exhibit
已刪除: simulation of
已刪除: when compared to
已刪除: 9c
已刪除: It is worth noting that in
已刪除: C–CTL, C–1day, C–3days, and C–6days, the variations in LHF
已刪除: underestimated.
已刪除: experiment C–18days, the variations in LHF are overestimated. In experiment
已刪除: 12days, the variations in LHF are similar to the expected values. The magnitude of SST fluctuations is directly related to the variations in LHF, FSNS, OLR, and U850
已移動 (插入) [8]
已設定格式: 字型色彩: 自動
已刪除: . In ERA5, phase 2 corresponds to the occurrence of the maximum positive SST anomaly within the domain of 110–130° E and 5–15° S, while phase 7 corresponds
已刪除: occurrence of the most negative SST anomaly. When comparing the high-frequency and low-frequency SST
已刪除: Additionally,
已刪除: occurrence of
已刪除: most negative SST anomaly aligns with the same
已刪除: the
已刪除: is
已刪除: the
已刪除: is
已刪除: MJO convection extracts heat (energy) from the
已刪除: **3 The**
已刪除: **of oceanic**
已刪除: **can sustain MJO propagation**

DeMott et al. (2014) noted that in uncoupled experiments, the NCAR CAM superparameterized version 3 (SPCAM3) exhibited strong eastward propagation when 5-day running mean SST was prescribed, but relatively weaker propagation for monthly mean SST. This raises the question of how much SST feedback periodicity is necessary to maintain robust eastward propagation in coupled experiments. This tendency was also seen in our study, that is, slower propagation (or weaker tendency) with decreased feedback frequency until the C–24days experiment (Figs. 1–7). By 1/30days, the perturbations became stationary.

Generally, C–18days exhibited the unrealistic overestimation of intraseasonal variability while maintaining eastward propagation of the MJO. Here, we are not suggesting that C–18days represents the optimal SST feedback experiment. Figure 8 highlights the considerable differences in the simulation of MJO perturbations at phase 2–3 in C–18days and C–30days experiments. In C–18days, negative OLR anomalies were widespread from the western Indian Ocean to the MC, while in reality it should be observed mainly in the Indian Ocean and be accompanied by positive anomalies in the eastern MC, i.e., a west-east dipolar structure (Fig. 8a). In C–30days, the OLR anomaly, although was still the dominant feature in the Indian Ocean-western Pacific region, became much weaker and characterized by smaller scale perturbations. These OLR anomalies were generally associated with upper-level convergence (not shown) embedded in much weaker wind anomalies (U200) compared to those in C–18days. The circulation and OLR in C–24days exhibited the characteristics similar to those in C–18days but with the OLR anomalies breaking up into smaller scales.

Furthermore, in the C–18days and C–24days experiments, positive anomalies in LHF and net surface heat flux (Fig. 8d, 8e, 8g, and 8h) were predominantly observed in the convection-inactive region to the east of 150°E where low-level easterly wind and negative SST anomalies prevailed (Fig. 8j). The OLR, winds, heat fluxes, and SST

已刪除: In previous studies, it has been observed that most models incorporate both coupled and uncoupled simulations.

已設定格式: 字型色彩: 文字 1

已刪除: specifically

已刪除: for

已刪除: means

已刪除: means

已刪除: This section aims to discuss this topic and explore strategies for achieving robust eastward propagation. It is observed that the aforementioned criteria are met with increased feedback periodicity for SST until the C–30days experiment. SST feedback periodicity, characterized by SST-forced atmospheric variability, exhibits notable differences between coupled and uncoupled experiments. In uncoupled experiments (A–CTL), the SST lacks responsiveness to atmospheric changes, leading to unrealistic intraseasonal variability in atmospheric circulation. Spatially, Through air–sea interaction, most of the coupled experiments showed improved MJO simulation with realistic strength and eastward propagation speeds (e.g., C–CTL, C–1day, C–3da...

已刪除: an

已刪除: 10

已刪除: robust (disordered) MJOs

已刪除: 4 between

已上移 [6]: 2022).

已刪除: are

已刪除: across the MC and extend to the WP near the equat...

已刪除: ocean to the atmosphere (Fig. 10g). Notably, in C–...

已刪除: at phase 2, the column-integrated vertical advectio...

已刪除: Generally, the -<wdmdp> accounts for ...

已刪除: further decomposed into variations of <wdmdp>, ...

已刪除: precipitation anomalies and

to the west of 150°E exhibited similar correspondences between variables but in opposite phase. With feedback frequency reduced to 1/30days (Fig. 8f, 8i, and 8l), the heat fluxes and SST anomalies broke into unorganized smaller scaler features, consistent with the ocean temperature shown in Fig. 6h. Although the wind fields in the both upper and lower levels were still characterized by large-scale structure, the corresponding divergence were dominated by much smaller scale perturbations (not shown), similar to heat fluxes and SST. The increasingly dominant smaller scale perturbations can also be inferred from Fig. 2h-j and 4h-j. In addition, the large power spectra in the low frequency band spread across a wide range of wavenumbers, reflecting the smaller scale nature of the simulated perturbations in C–30days (Fig. 3h-j). This imparity between the scale of rotational and divergent winds suggests that the poor coupling between the convection and large-scale circulation.

With decreased feedback frequency of SST from C–CTL to C–30days, the ocean continued to receive atmospheric forcing, but the feedback response was delayed, leading to the accumulation or loss of energy (temperature) in the upper ocean, as seen in the SST distribution in the WP (Fig. 6 and 8). Subsequently, the C–30days experiment exhibited comprehensive disorder over the Indo-Pacific region, with the SST exhibiting a perturbed unrealistically spatial distribution (Fig. 8l) associated with plus-minus latent heat flux and 10m wind anomalies (Fig. 8f), net surface heat flux, and solar radiation (Fig. 8i). As a result, the organized large-scale circulation seen in the MJO was not manifested. To this extreme, the air–sea interaction observed in the MJO no longer worked properly in the model.

4.3 Moist static energy (MSE) budget analysis

We diagnosed the relative contribution of each term in Eq. (1) to the MSE tendency with a focus on the second (pre-conditioning) and fifth (convection crossing the MC) phases. Figure 9 illustrates the physical processes associated with each term (averaged over 10° S–0°, 120–150° E) contributing to the column-integrated MSE tendency (<dmdt>) in Eq. (1) during phase 2 in ERA5 and model simulations. In ERA5, when the MJO convection was in the eastern Indian Ocean, the column-integrated vertical and horizontal advection (-<wdmdp> and -<vdm>) over the MC area were the dominant terms in the MSE budget and largely compensated by longwave radiation and latent heat flux, as reported in Wang and Li (2020) and Tseng et al. (2022). All experiments simulated the positive and negative contributions similar to those derived from ERA5 although with different amplitudes. Notably, the C–24days and C–30days simulated relatively weak vertical advection and too strong negative latent heat flux and too weak longwave radiation flux. As a result, the C–24days and C–30days simulated relatively weak tendency compared to other experiments. The results are consistent with the poor simulation of the MJO in the extreme low frequency feedback experiments discussed above.

We compared the spatial distribution of column-integrated MSE tendency <dmdt> (shading), precipitation (contours), and 850-hPa wind (vectors) during phase 5, i.e., the period when the strongest convection crossing the MC (Fig. 10). In ERA5, the main convection (indicated by positive precipitation anomaly) is accompanied by low-level convergence in the 850-hPa wind across the MC extending into the WP (Fig. 10a). A positive <dmdt> is observed to the east of the MJO convection to the south of the equator (Fig. 10a). Conversely, a negative tendency is observed to the west of the MJO convection accompanied by negative precipitation anomalies further to the west. The phase relationship between the MSE tendency and precipitation reflects the eastward-propagating nature of the MJO. With the exception of A–CTL, C–24days, and C–30days, the model simulations displayed a similar structure in the 20–100-day filtered <dmdt>, precipitation, and 850-hPa wind vectors (Fig. 10c–h). although the exact

格式化: 左右對齊

已刪除: 12a

已刪除: MSE tendency, peaking near 15° N and 15° S,

已刪除: located near

已刪除: Equator.

已刪除: integrated MSE

已刪除: of this region. The meridionally confined structure near the Equator exhibits characteristics indicative of an equatorial Kelvin wave propagated toward the east as fundamental dynamics of the MJO.

已刪除: display

已刪除: to ERA5

已刪除: terms of

已刪除: 12c–h). C–CTL exhibits relatively weak precipitation anomalies in the MC and weak westerly winds in the IO until C–6days, where robust precipitation and low-level convergence in the 850-hPa wind occur in response to the feedback periodicity of SST increasing. On the contrary, A–CTL exhibits abnormal positive precipitation anomalies distributed over the western IO, while localized maximum of <dmdt> occur near 15° N (Fig. 12b). In contrast, C–30days displays plus-minus precipitation anomalies near the Equator, consequently disrupting the spatial distribution of the <dmdt> relative to MJO convection (Fig. 12i).

locations may be shifted compared to those derived from ERA5. The C–CTL simulated relatively weak signals compared to ERA5, whereas the signals became increasingly stronger with decreasing feedback frequency. The signals became unrealistically strong beyond 1/18days feedback frequency and the lead–lag relationship between the MSE tendency and precipitation became less clear. For example, positive precipitation anomaly became in phase with the tendency in the western Pacific south of the equator in C–24days and C–30days experiments, and the tendency was much weaker in C–30days. The results were consistent with the weaker eastward propagation tendency in the low-frequency feedback experiments, especially in C–24days and C–30days when the feedback frequency became unrealistically low.

The corresponding MSE budget during phase 5 is shown in Fig. 10. The MC has been identified as a barrier to the eastward propagation of the MJO (Hsu and Lee, 2005, Wu and Hsu 2009, Tseng et al. 2017, Li et al., 2020b) and approximately 30–50% of the MJO experienced stalling over the MC (Zhang and Han, 2020). To determine whether the MJO has sufficient energy to traverse the MC, we focused the analysis on phase 5. Figure 11 illustrates the projection of each MSE component and decomposition of the horizontal MSE advection at phase 5 over the MC region (20° S–20° N, 90–210° E) following the approach of Tseng et al. (2022) and Jiang et al. (2018), where F_s is total surface fluxes including SH and LH, and Q_r is vertically integrated net SW and LW radiation. Unlike in phase 2 when vertical advection is the dominant term, the MSE tendency was dominated by the horizonal MSE advection -<vdm> in ERA5 and all experiments, except the A–CTL. This contribution increased with decreasing SST feedback frequency. The weaker positive vertical advection -<wdmdp> did not vary systematically with decreasing feedback frequency and even turned negative in C–24days and C–30days. Fs and Qr acted to damp the tendency by cancelling out the effect of the advection term. Fs tended to be more negative with decreasing feedback

已刪除: To quantify the impact of SST feedback periodicity on atmospheric intraseasonal variability in the tropics, we adopt the approach of Tseng et al. (2022) and Jiang et al. (2018) to project all MSE terms onto the 20–100-day filtered ERA5 <dmdt> (Fig. 12a)

已刪除: .

已刪除: frequently

已刪除: , as noted by

已刪除: . (

已刪除:). Additionally, a considerable proportion,

已刪除: %,

已刪除: experiences

已刪除: , as reported by

已刪除: (

已刪除: mitigate

已刪除: influence of weaker

已刪除: events that dissipate prior to reaching

已刪除: our focus is specifically

已刪除: of the MJO

已刪除: 13(a)

已刪除: determination of the contribution

已刪除: tendency during

已刪除: by projecting the spatial pattern of each MSE budget term

已刪除: sensible

已刪除: latent heat fluxes

已刪除: radiative (short-wave and long-wave) heat fluxes. The

已刪除: contribution of horizontal advection to the MSE ...

已刪除: is not the dominant term over the MC region (20° S ...

已刪除: make a minor contribution to the MSE tendency, ...

frequency and became much larger in C–30days. By contrast, Qr was unrealistically weak in C–18days, C–24days, and C–30days. The uncoupled simulation yielded much weaker amplitude in all terms as expected.

The -<vdm> that contributed most to the eastward propagation of the MJO in phase 5 was further decomposed into zonal (-<udmdx>) and meridional (-<vdmdy>) components to examine their relative effects (Fig. 11). Both components contributed positively, but the -<vdmdy> exhibited a larger amplitude, consistent with Tseng et al. (2014, 2022). The -<vdmdy> of high-frequency SST feedback experiments yielded results closely similar to ERA5. Comparatively, the -<vdmdy> term in low-frequency SST feedback experiments (C–18days, C–24days, and C–30days) became unrealistically large with decreasing feedback frequency.

Spatial distributions of -<wdmdp>, -<vdm>, and 200-hPa wind at phase 5 are shown in Fig. 12. In ERA5, the wind divergence at 200 hPa at phase 5 (Fig. 12a), overlaid the 850-hPa convergence (Fig. 10a), reflecting a deep convection structure. The model simulations exhibited a similar structure to ERA5 except in A–CTL, C–24days, and C–30days experiments, and again the amplitude increased with decreasing feedback frequency. In ERA5, negative -<wdmdp> and -<vdm> anomalies (Fig. 12a) were observed to the west of the MJO convection (Fig. 10a). The spatial distribution of the negative -<vdm> anomaly (dashed-red contours) extends from the IO to the MC and positive anomaly (predominantly meridional advection from the south, not shown) in the western-central Pacific south of the equator tends to facilitate the eastward propagation of deep convection in the western Pacific, consistent with Tseng et al. (2014, 2022). The -<wdmdp> with negative and positive anomaly to the west and east of the deep convection also contributes to the eastward propagation of the MJO, but with weaker contribution than -<vdm>. Again, these characteristics were not simulated in A-CTL, whereas the amplitudes of both terms became increasingly larger with

已刪除: response to the increasing feedback periodicity of SST.
…–18days, C–24days, and C–30days. The total horizontal MSE advection is

格式化: 左右對齊

已刪除: its …onal (-<udmdx>) and meridional zonal …-<vdmdy>) components for high-frequency SST feedback experiments (C–CTL, A–CTL, C–1day, and C–3days) and low-frequency SST feedback experiments (C–6days, C–12days, C–18days, and C–30days) in order

已刪除: individual…elative effects (Fig. 13b–c…1). Both components contribute…ontributed positively, but the -<vdmdy> exhibits…xhibited a larger amplitude, consistent with findings by …seng et al. (2014, 2022) during phase 4.

已刪除: (C–CTL, C–1day, and C–3days) …ielded results closely resemble ERA5 in terms of the projected magnitude

已刪除: 6days, C–12days, C–…8days, and C–30days) exhibits a more positive contribution than in high-frequency SST experiments, leading to a dominant contribution to the increase in -<vdm> and <dmdt>.

已刪除: We generated a spatial representation…patial distributions of the 20–100-day column-integrated vertical MSE advection (J kg^{-1} s^{-1}, represented by shading), column-integrated horizontal MSE advection (J kg^{-1} s^{-1}, shown as contours with an interval of 6.0),…<wdmdp>, -<vdm>, and 200-hPa wind (green vectors) relative to a reference vector (3 m s^{-1}) during …t phase 5 (Fig. 14). This figure complements the information provided by the bar chart …re shown in Fig. 13a…2. In ERA5, the wind divergence at 200 hPa during…t phase 5 (Fig. 14a…2a), overlaid with …he 850-hPa convergence (Fig. 12a), indicates a vertically tilting…0a), reflecting a deep convection structure of zonal wind anomalies. Except for A–CTL and C–30days, the … The simulations exhibit…xhibited a similar structure to ERA5 in terms of low-level convergence and high-level divergence.…xcept in A–CTL, C–24days, and C–30days experiments, and again the amplitude increased with decreasing feedback frequency until becoming unrealistically large beyond 1/18days. In C–30days experiment both terms exhibited unorganized spatial structure as shown in preceding discussion. In summary, the high-frequency feedback experiments simulated an approximately 80% projection of -<vdm> in ERA5, whereas the low-frequency SST feedback experiments overestimated -<vdm> anomalies (Fig. 12f–h).

5. Conclusions

This study built upon the work of Lan et al. (2022) and Tseng et al. (2022) by coupling a high-resolution 1-D TKE ocean model (the SIT model) with the CAM5, i.e., a CAM5–SIT configuration, to investigate the effects of intraseasonal SST feedback on the MJO. We introduced asymmetric exchange frequencies between the atmosphere and the ocean, ensuring bidirectional interaction at each timestep within the experimental periodicity by fixing the SST value in the coupler. This allowed us to create SST feedback with various intervals at 30 minutes, 1, 3, 6, 12, 18, 24, and 30 days.

The aim is to assess the effect of SST feedback frequency, namely, how often should the atmosphere-driven SST change feedback to the atmosphere and whether there is a limit. With the exception of the C–24days and C–30days experiment, both the high-frequency and low-frequency experiments demonstrated realistic simulations of various aspects of the MJO when compared to ERA5, GPCP, and OISST data, although the simulation results becoming increasingly amplified and unrealistic with decreasing feedback frequency. These aspects included intraseasonal periodicity (Fig. 1), eastward propagation (Fig. 2 and 4), coherence in the intraseasonal band (Fig. 3), tilting vertical structure (Fig. 5), intraseasonal SST (Table 2) and oceanic temperature variances (Fig. 6), the lead–lag relationship of intraseasonal variability (Fig. 7), contribution of each term to the column-integrated MSE tendency at the preconditioning phase (phase 2) and mature phased (phase 5) (Fig. 9 and Fig. 11). The MSE tendency term was

已刪除: , the positive -<vdm> anomaly (solid-blue contours) exhibits a spatial distribution near 120° E (Fig. 14b), while the negative -<vdm> anomaly (dashed-red contours) is distributed on both the positive left and right sides. Although the negative -<vdm> anomaly in high-frequency SST feedback experiments (C–CTL, C–1day, and C–3days) underestimates that of ERA5 (Fig. 14c–e), the spatial distribution remains similar to ERA5 due to…both terms exhibited unorganized spatial structure as shown in preceding discussion. In summary, the high-frequency feedback experiments simulated an approximately 80% projection of -<vdm> compared to ERA5. The low-frequency SST feedback experiments (C–6days, C–12days, and C–18days) yield ...

已刪除: , although the anomalies of -<wdmdp> intensify, the spatial distribution of those shift eastward, leading to a decrease in projection values.

已刪除: builds…uilt upon the work of Lan et al. (2022) and Tseng et al. (2022) by coupling a high-resolution 1-D TKE ocean model (the SIT model) with the CAM5, specifically ...

已刪除: of…t 30 minutes, 1, 3, 6, 12, 18, 24, and 30 days. Systematic sensitivity experiments were conducted to divide to divide into two groups: those feedback periodicity within ...

已刪除: scientific reproducibility and consistency…ffect of the findings across different …ST feedback cycles in the field of modeling science.…requency, namely, how often should ...

已刪除: …. GPCP, and OISST data, although the simulation results becoming increasingly amplified and unrealistic with decreasing feedback frequency. These aspects include ...

已刪除: as shown in

已刪除: as observed in …ig. 2 and 4), coherence in the low-frequency …ntraseasonal band (as depicted in ...

已刪除: evident in …ig. 5, 12, and 14 for zonal wind ...

已刪除: as summarized in …able 2) and oceanic temperature variances (as shown in …ig. 7…), the lead–lag relationship of intraseasonal variability (as characterized in …ig. 9), phase ...

dominated by the horizonal and vertical MSE advection in phase 5 and phase 2, respectively, in ERA5 and most experiments. Furthermore, we deliberately extended the SST feedback interval to an unrealistically long 30 days to investigate the limits of delayed ocean response. The main conclusion is less frequent the update, more unrealistic the simulation result.

The lead–lag relationship provides a visual representation of the variations in 20–100-day filtered LHF, FSNS, OLR, U850 and SST with positive SST anomaly leading the onset of the MJO convection (Fig. 7). This relationship highlights the interconnected nature of surface heat fluxes, solar radiation, and atmospheric circulation patterns, underscoring their mutual influence and interplay through air–sea interaction. Our results indicate that the high-frequency (low-frequency) SST experiments tended to underestimate (overestimate) the MJO simulation in CAM5–SIT model. Whether this finding can be applied to other models warrants further investigations.

The result of C–3days experiment is consistent with Stan (2018), suggesting the absence of 1–5-day variability in SST would promote the amplification of westward power associated with tropical Rossby waves. By comparing with the control experiment in which SST feedback occurs at every time step (30 minutes), the C–1day experiment (SST feedback once daily) confirmed the findings of Hagos et al. (2016) and Lan et al. (2022) that the removal of the diurnal cycle would enhance the MJO. The increasing feedback periodicity of SST in low-frequency experiments led to the accumulation of atmospheric influences through short-wave and long-wave radiations and surface heat fluxes, resulting in an unrealistically large ocean temperature anomalies and variances within few tens of meters below ocean surface (Table 2). The large-scale nature of the MJO remains intact with decreasing feedback frequency, although becoming increasingly unrealistic in both structure and amplitude, until

已删除: , while

已删除: up to

已删除: 9

已删除: oceanic

已删除: . Table 3 provides a comprehensive overview of several variables during the boreal winter, including the average values of 20–100-day filtered OLR, LHF, FSNS, U850, <dmdt>, -<wdmdp>, and -<vdm>. These variables are categorized based on the states of SST warming and cooling. The categorization is performed over two specific domains: (110–130° E, 5–15° S), as referenced in Fig. 9, and (120–150° E, 0–10° S) marked as background gray, as referenced in Fig. 11. We highlight the characteristics of the MJO-related atmosphere with red letters, which correspond closely to the values in ERA5. In synthesizing the findings from Arnold et al. (2013) regarding the high SST enhances MJO simulation, the improved MJO simulation through intraseasonal SST variability by Liang et al. (2018), the information provided ...

已删除: . Notably, the experiment C–6days demonstrated th ...

已删除: Among the high-frequency experiments, C–3days ...

已删除: the

已删除: as

已删除: promotes

已删除: In addition,

已删除: confirms the scientific reproducibility

已删除: demonstrates that

已删除: enhances

已删除: ...

已删除: leads

已删除: from the atmosphere

已删除: increase in the upper oceanic temperature and its ...

已删除: spatial distribution and an

已删除: vertical tilting

1/30days when the intraseasonal fluctuations were overwhelmingly dominated by unorganized small scale perturbations in both atmosphere and ocean, as well as at the atmosphere-ocean interface where heat and energy were rigorously exchanged.

The reason causing the sudden change between C–24days and C–30days is not entirely clear. Two possibilities are discussed here. The first possible reason leading to this disorder is that when the ocean feedback is delayed for as long as 30 days (more than half of the MJO period) both positive and negative fluxes would contribute to the heat accumulation or loss in the ocean because of the MJO phase transition and result in unorganized small scale structures in ocean temperatures, which could in turn affect the heat flux and convection. The second would be the SST change become more abrupt and disrupt the large-scale nature of the MJO. However, whether large-amplitude SST fluctuations would induce unorganized small-scale pertrubation is debatable. As seen in many hypothetic (or theoretical) studies, a sudden initiation of SST (or step-function like) could induce large scale responses. This issue remains an open question that warrants further studies with purposedly designed expeirment to untangle.

Finally, results of intraseasonal SST feedback experiments on MJO are summarized schematically in Fig. 13, following DeMott et al. (2014). These experiments included the uncoupled experiment (A–CTL), high-frequency SST experiments (C–CTL, C–1day, and C–3days), low-frequency SST experiments (C–6days, C–12days, C–18days), and extreme low-frequency experiment (C–24days and C–30days). In the absence of intraseasonal SST variability, the eastward propagation of the MJO was disrupted, leading to weakened or fragmented MJO activity as shown in Fig. 13a. On the other hand, the high-frequency SST experiments closely mimicked air–sea interaction and well captured the characteristics of the MJO. The time-varying SSTs in the coupled simulation provided a certain degree of organization and sufficient surface fluxes, which facilitated the development of the MJO circulation as illustrated

已刪除: specific humidity and air temperature anomalies (Fig. 5i) over the Indo-Pacific region. As a result, local convection appears randomly among the IO, MC, and WP, and does not manifest as organized MJO convection

已刪除: in Fig. 15, the interseasonal

格式化: 左右對齊

已刪除: depicted

已刪除: .

已刪除: include

已刪除: model

已刪除: disorganized convection

已刪除: circulation (

已刪除:) which figure concept is based on DeMott et al. (2014) in Fig. 11.

已刪除: interseasonal

已刪除: uncoupled A–CTL disrupts the

已刪除: 15a

已刪除: generally capture

已刪除: provide

已刪除: level

已刪除: facilitate

已刪除: circulations,

in Fig. 13b. The horizontal moist static energy tendency derived from increased low-level convergence, especially due to the meridional advection of MSE, intensified the MJO convection and triggered the eastward propagation over the MC region. The PBL convergence ahead of the MJO convection is due to Kelvin-wave dynamics (Jiang, 2017), in conjunction with the background zonal flow structure (Tulich and Kiladis, 2021). Horizontal MSE or moisture advection in the lower troposphere, particularly the seasonal mean low-level MSE influenced by the MJO's anomalous winds, has had a significant impact on the MJO propagation. (Gonzalez and Jiang, 2017; Jiang, 2017). This simulation result is consistent with the understanding that the MJO is primarily attributed to the interaction between organized convection and large-scale circulations that triggers the eastward propagation. As feedback frequency become lower, the major characteristics of the MJO could still be simulated as depicted in Fig. 13c, but with overestimated amplitudes and deteriorating simulations in spatial structures. In the extreme low frequency experiments with frequency decreasing to 1/24days and 1/30days, unorganized structures started to emerge and broke up into smaller scale perturbations as shown in Fig. 13d, when proper air–sea interaction did not operate properly in the model. Eventually in the C–30days experiment, unrealistically and spatially scattered anomalies in precipitation, SST, surface heat fluxes, and vertical and horizontal MSE advection became dominant features. All these findings led to the major conclusion of this study: spontaneous atmosphere-ocean interaction with high resolution ocean model is a key to the proper simulation of the MJO in the climate models.

Code and data availability. The model code of CAM5–SIT is available at https://doi.org/10.5281/zenodo.5510795. Input data of CAM5–SIT using the climatological Hadley Centre Sea Ice and Sea Surface Temperature dataset and

已删除: 15b. Moreover, in the coupled model, the presence of land convection over the MC ahead of the MJO convection (Fig. 6) contributes to the instability and uplift of

已删除: air masses. Conventionally, the MJO has been regarded as a tropical atmospheric variability, given that its existence is primarily attributed to the interplay between organized convection and large-scale circulations. This dynamic process plays a crucial role in triggering

已删除: of the MJO. Furthermore, the low-frequency SST experiments demonstrate robust simulations of the MJO. This can be attributed comprehensively

已删除: the increased SST variances, accumulation of surface fluxes, enhanced low-level convergence (Fig. 12) and high-level divergence (Fig. 14), as well as horizontal

已删除: , as depicted in Fig. 15c. On the other hand, the C–30days experiment simulates frequent, disorganized convection,

已删除: 15d. This experiment exhibits both positive and negative

已删除: , which fail to generate the expected circulation anomalies

GODAS data forcing, including 30-year numerical experiments, are available at https://doi.org/10.5281/zenodo.5510795.

Author contributions. YYL is the CAM5–SIT model developer and writes the majority part of the paper. HHH contributes to the physical explanation and the reorganization and revision of the manuscript. WLT assists in the MSE analysis.

已刪除: HHH is the initiator and the primary investigator of the Taiwan Earth System Model project.

Competing interests. The authors declare that they have no conflict of interest.

Acknowledgements. The contribution from YYL, HHH, and WLT to this study is supported by the Ministry of Science and Technology of Taiwan under MOST 110-2123-M-001-003, MOST 110-2811-M-001-603, MOST 109-2811-M-001-624 and MOST108-2811-M-001-643. Our deepest gratitude goes to the editors and anonymous reviewers for their careful work and thoughtful suggestions that have helped improve this paper substantially. We sincerely thank the National Center for Atmospheric Research and their Atmosphere Model Working Group (AMWG) for release CESM1.2.2. We thank the computational support from National Center for High530 performance Computing of Taiwan. Thanks, ChatGPT for correcting the English grammar.

已刪除: contracts

已刪除: 分頁符號

格式化: 左右對齊

Reference

Adler, R. F., Huffman, G. J., Chang, A., Ferraro, R., Xie, P. P., Janowiak, J., Rudolf, B., Schneider, U., Curtis, S., Bolvin, D., Gruber, A., Susskind, J., Arkin, P., and Nelkini, E.: The Version 2.1 Global Precipitation Climatology Project (GPCP) Monthly Precipitation Analysis (1979 -Present), J. Hydrometeor., 4(6), 1147-1167, https://doi.org/10.1175/1525-7541(2003)004<1147:TVGPCP>2.0.CO;2, 2003.

Amante, C., and Eakins, B. W.: ETOPO1 1 arc-minute globe relief model: Procedures, data sources and analysis, NOAA Tech. Memo. NESDIS

NGDC-24, NOAA, Silver Spring, MD, 19 pp., https://doi.org/10.7289/V5C8276M, 2009.

Banzon, V. F., Reynolds, R. W., Stokes, D., and Xue, Y.: A 1/4-spatial-resolution daily sea surface temperature climatology based on a blended satellite and in situ analysis, J. Climate, 27, 8221–8228, https://doi.org/10.1175/JCLI-D-14-00293.1, 2014.

Behringer, D. W., and Xue, Y.: Evaluation of the global ocean data assimilation system at NCEP: The Pacific Ocean. Eighth Symposium on Integrated Observing and Assimilation Systems for Atmosphere, Oceans, and Land Surface, AMS 84th Annual Meeting, Washington State Convention and Trade Center, Seattle, Washington, 11-15. Derber, J.C., and A. Rosati, 1989: A global oceanic data assimilation system, J. Phys. Oceanogr., 19, 1333–1347, https://ams.confex.com/ams/pdfpapers/70720.pdf, 2004.

Chang, M.-Y., Li, T., Lin, P.-L., and Chang, T.-H.: Forecasts of MJO Events during DYNAMO with a Coupled Atmosphere-Ocean Model: Sensitivity to Cumulus Parameterization Scheme, J. Meteorol. Res., 33, 1016–1030, https://doi.org/10.1007/s13351-019-9062-5, 2019.

CLIVAR MADDEN–JULIAN OSCILLATION WORKING GROUP: MJO simulation diagnostics, J. Climate, 22, 3006–3030, https://doi.org/10.1175/2008JCLI2731.1, 2009.

DeMott, C. A., Klingaman, N. P., and Woolnough, S. J.: Atmosphere-ocean coupled processes in the Madden-Julian oscillation, Rev. of Geophysics, 53, 1099– 1154, https://doi.org/10.1002/2014RG000478, 2015.

DeMott, C. A., Stan, C., Randall, D. A., and Branson, M. D.: Intraseasonal variability in coupled GCMs: The roles of ocean feedbacks and model physics, J. Climate, 27(13), 4970– 4995. https://doi.org/10.1175/JCLI-D-13-00760.1., 2014.

de Szoeke, S. P., Edson, J. B., Marion, J. R., Fairall, C. W., and Bariteau, L.: The MJO and air–sea interaction in TOGA COARE and DYNAMO, J. Climate, 28(2), 597– 622. https://doi.org/10.1175/JCLI-D-14-00477.1, 2014.

de Szoeke, S. P., Edson, J. B., Marion, J. R., Fairall, C. W., and Bariteau, L.: The MJO and air–sea interaction in TOGA COARE and DYNAMO, J. Climate, 28, 597–622, https://doi.org/10.1175/JCLI-D-14-00477.1, 2015.

de Szoeke, S. P., and Maloney, E.: Atmospheric mixed layer convergence from observed MJO sea surface temperature anomalies, J. Climate, 33(2), 547– 558. https://doi.org/10.1175/JCLI-D-19-

已下移 [9]: . P.,

已刪除: Arnold, N

已刪除: Kuang, Z., and Tziperman, E.: Enhanced MJOlike variability at high SST, J. Climate, 26, 988–1001, https://doi.org/10.1175/JCLI-D-12-00272.1, 2013.

已設定格式: author, 字型色彩: 文字 1, 圖樣:清除 (白色)

已刪除: de Boisséson, E., Balmaseda, M. A., Vitart, F., and Mogensen, K.: Impact of the sea surface temperature forcing on hindcasts of Madden-Julian Oscillation events using the ECMWF model, Ocean Sci., 8, 1071–1084, https://doi.org/10.5194/os-8-1071-2012, 2012.

已設定格式: 圖樣:清除 (白色)

已設定格式: 預設段落字型, 字型色彩: 自動, 圖樣:清除

已設定格式: 圖樣:清除

格式化: 左右對齊

已移動 (插入) [9]

已設定格式: author, 字型色彩: 文字 1, 圖樣:清除 (白色)

0351.1, 2020.

Fu, J. X., Wang, W., Shinoda, T., Ren, H. L., and Jia, X.: Toward understanding the diverse impacts of air–sea interactions on MJO simulations, J. Geophys. Res.-Oceans,122(11), 8855– 8875. https://doi.org/10.1002/2017JC013187, 2017.

Gao, Y., Hsu, P.-C., Chen, L., Wang, L., and Li, T.: Effects of high-frequency surface wind on the intraseasonal SST associated with the Madden-Julian oscillation, Clim. Dynam., 54, 4485–4498, https://doi.org/10.1007/s00382-020-05239-w, 2020a.

Gao, Y., Klingaman, N. P., DeMott, C. A., and Hsu, P.-C.: Boreal summer intraseasonal oscillation in a superparameterized general circulation model: effects of air–sea coupling and ocean mean state, Geosci. Model Dev., 13, 5191–5209, https://doi.org/10.5194/gmd-13-5191-2020, 2020b.

Ge, X., Wang, W., Kumar, A., and Zhang, Y.: Importance of the vertical resolution in simulating SST diurnal and intraseasonal variability in an oceanic general circulation model, J. Climate, 30, 3963–3978, https://doi.org/10.1175/JCLI-D-16-0689.1, 2017.

Gonzalez, A. O., and Jiang, X.: Winter mean lower tropospheric moisture over the maritime continent as a climate model diagnostic metric for the propagation of the Madden-Julian Oscillation, Geophys. Res. Lett., 44(5), 2588–2596. https://doi.org/10.1002/2016GL072430, 2017.

Hagos, S. M., Zhang, C., Feng, Z., Burleyson, C. D., Mott, C. De, Kerns, B., Benedict, J. J., and Martini, M. N.: The impact of the diurnal cycle on the propagation of Madden-Julian Oscillation convection across the Maritime Continent, J. Adv. Model. Earth Syst., 8, 1552–1564, https://doi.org/10.1002/2016MS000725, 2016.

Hersbach, H., and Dee, D.: ERA5 reanalysis is in production, ECMWF Newsletter, Vol. 147, p. 7, https://www.ecmwf.int/en/newsletter/147/news/era5-reanalysis-production, 2016.

Hong, X., Reynolds, C. A., Doyle, J. D., May, P., and O'Neill, L.: Assessment of upper-ocean variability and the Madden-Julian Oscillation in extended-range air–ocean coupled mesoscale simulations, Dyn. Atmos. Oceans, 78, 89–105. https://doi.org/10.1016/j.dynatmoce.2017.03.002, 2017.

Hsu, H.-H., and Lee, M.-Y.: Topographic effects on the eastward propagation and initiation of the Madden-Julian Oscillation, J. Climate, 18, 795-809, https://doi.org/10.1175/JCLI-3292.1, 2005.

Hurrell, J. W., Holland, M. M., Gent, P. R., Ghan, S., Kay, J. E., Kushner, P. J., Lamarque, J.-F., Large, W. G., Lawrence, D., Lindsay, K., Lipscomb, W. H., Long, M. C., Mahowald, N., Marsh, D. R., Neale,

已下移 [10]: Adv. Model. Earth Syst.,

已刪除: Fuchs, Ž., and Raymond, D. J.: A simple model of intraseasonal oscillations, J.

已下移 [11]: Hagos, S. M., Zhang, C., Feng, Z., Burleyson, C. D., Mott, C. De, Kerns, B., Benedict, J. J., and Martini, M. N.: The impact of the diurnal cycle on the propagation of Madden-Julian Oscillation convection across the Maritime Continent, J. Adv. Model. Earth Syst., 8, 1552–1564, https://doi.org/10.1002/2016MS000725, 2016. Hersbach, H., and Dee, D.: ERA5 reanalysis is in production, ECMWF Newsletter, Vol. 147, p. 7, https://www.ecmwf.int/en/newsletter/147/news/era5-reanalysis-production, 2016.

已刪除: 9, 1195–1211. https://doi.org/10.1002/2017MS000963, 2017.

已移動 (插入) [12]

已設定格式: 圖樣:清除 (白色)

已移動 (插入) [11]

格式化: 左右對齊

已設定格式: 字型色彩: 自動

已刪除: J.-Y., Hendon,

已設定格式: 字型色彩: 自動

已刪除: ., Feng, M

已設定格式: 字型色彩: 自動

已設定格式: 字型色彩: 自動

已刪除: Zhou, X.: Magnitude

已設定格式: 字型色彩: 自動

已刪除: phase

已設定格式: 字型色彩: 自動

已刪除: diurnal SST variations in the access-S1 model during

已設定格式: 字型色彩: 自動

已刪除: suppressed phase of the MJOs, J. Geophys. Res.-Oceans, 124 (2019), pp. 9553-9571

已設定格式: 字型色彩: 自動

已設定格式: apple-converted-space, 字型色彩: 黑色, 圖樣:清除

已刪除: 1029/2019JC015458, 2019

已設定格式: 字型色彩: 自動

已設定格式: 字型色彩: 自動, 圖樣:清除

R. B., Rasch, P., Vavrus, S., Vertenstein, M., Bader, D., Collins, W. D., Hack, J. J., Kiehl, J., and Marshall, S.: The Community Earth System Model: A framework for collaborative research, Bull. Amer. Meteor. Soc., 94, 1339–1360, https://doi.org/10.1175/BAMS-D-12-00121.1, 2013.

Jiang, X.,Waliser, D. E., Xavier, P. K., Petch, J., Klingaman, N. P., Woolnough, S. J., Guan, B., Bellon, G., Crueger, T., DeMott, C., Hannay, C., Lin, H., Hu, W., Kim, D., Lappen, C.-L., Lu, M.-M., Ma, H.-Y., Miyakawa, T., Ridout, J. A., Schu-bert, S. D., Scinocca, J., Seo, K.-H., Shindo, E., Song, X., Stan, C., Tseng, W.-L., Wang, W., Wu, T., Wu, X., Wyser, K., Zhang, G. J., and Zhu, H.: Vertical structure and physical processes of the MaddenJulian oscillation: Exploring key model physics in climate simulations, J. Geophys. Res.-Atmos., 120, 4718–4748, https://doi.org/10.1002/2014JD022375, 2015.

Jiang, X.: Key processes for the eastward propagation of the Madden-Julian Oscillation based on multimodel simulations, J. Geophys. Res. Atmos., 122, 755–770, https://doi.org/10.1002/2016JD025955, 2017.

Jiang, X., Adames, Á. F., Zhao, M., Waliser, D., and Maloney, E.: A unified moisture mode framework for seasonality of the Madden–Julian oscillation, J. Climate, 31, 4215–4224, https://doi.org/10.1175/JCLI-D-17-0671.1, 2018.

Jiang, X., Adames, Á. F., Kim, D., Maloney, E. D., Lin, H., and Kim, H., Zhang, C., DeMott, C. A., and Klingaman, N. P.: Fifty years of research on the Madden-Julian Oscillation: Recent progress, challenges, and perspectives, J. Geophys. Res.-Atmos., 125, e2019JD030911, https://doi.org/10.1029/2019JD030911, 2020.

Kim, D., Kim, H., and Lee, M.-I.: Why does the MJO detour the Maritime continent during Austral summer? Geophys. Res. Lett., 44(5), 2579–2587, https://doi.org/10.1002/2017gl072643, 2017.

Kim, H., Vitart, F., and Waliser, D. E.: Prediction of the Madden–Julian oscillation: A review, J. Climate, 31(23), 9425– 9443, https://doi.org/10.1175/JCLI-D-18-0210.1, 2018.

Klingaman, N. P., and Demott, C. A,: Mean state biases and interannual variability affect perceived sensitivities of the Madden-Julian oscillation to air–sea coupling, J. Adv. Model. Earth Syst., 12, 1– 22, https://doi.org/10.1029/2019MS001799, 2020.

Krishnamurti, T. N., Oosterhof, D. K. and Mehta, A. V.: Air–sea interaction on the time scale of 30 to 50 days, J. Atmos. Sci., 45, 1304–1322, https://doi.org/10.1175/1520-0469(1988)045,1304:AIOTTS.2.0.CO;2, 1988.

Lambaerts, J., Lapeyre, G., Plougonven, R., and Klein, P.: Atmospheric response to sea surface temperature mesoscale structures, J. Geophys. Res.-Atmos., 118(17), 9611–9621.

已移動 (插入) [13]

已刪除: Hsu, P.-C., and Li, T.: Role of the boundary layer moisture asymmetry in causing the eastward propagation of the Madden–Julian oscillation, J. Climate, 25:4914–4931, https://doi.org/10.1175/JCLI-D-11-00310.1, 2012. Jayakumar, A., Vialard, J., Lengaigne, M., Gnanaseelan, C., McCreary, J.P., and Kumar, B.P.: Processes controlling the surface temperature signature of the Madden-Julian oscillation in the thermocline ridge of the Indian Ocean,

已設定格式: 圖樣:清除 (自訂色彩(RGB(252,252,252)))

已下移 [14]: Clim.

已設定格式: 預設段落字型, 字型色彩: 自動, 圖樣:清除

已刪除: Dynam., 37, 2217–2234, https://doi.org/10.1007/s00382-010-0953-5, 2011.

已移動 (插入) [15]

已設定格式: 圖樣:清除 (白色)

格式化: 左右對齊

已刪除: Kang, D.,

已刪除: Ahn, M. S., Neale, R., Lee, J

已移動 (插入) [16]

已刪除: Gleckler, P. J.: The role of

已刪除: mean state on

已刪除: simulation in CESM2 ensemble simulation,

已刪除: 47, e2020GL089824.

已刪除: 1029/2020GL089824, 2020

https://doi.org/10.1002/jgrd.50769, 2020.

Lan, Y.-Y., Hsu, H.-H., Tseng, W.-L., and Jiang, L.-C.: Embedding a one-column ocean model in the Community Atmosphere Model 5.3 to improve Madden–Julian Oscillation simulation in boreal winter, Geosci. Model Dev., 15, 5689–5712, https://doi.org/10.5194/gmd-15-5689-2022, 2022.

Li, Y., Han, W., Shinoda, T., Wang, C., Ravichandran, M., and Wang, J.-W.: Revisiting the wintertime intraseasonal SST variability in the tropical south Indian Ocean: Impact of the ocean interannual variation, J. Phys. Oceanogr., 44, 1886–1907, https://doi.org/10.1175/JPO-D-13-0238.1, 2014.

Li, T., Ling, J., and Hsu, P.-C.: Madden–Julian Oscillation: Its discovery, dynamics, and impact on East Asia, J. Meteor. Res., 34, 20–42, https://doi.org/10.1007/s13351-020-9153-3, 2020a.

Li, K., Yu, W., Yang, Y., Feng, L., Liu, S., and Li, L.: Spring barrier to the MJO eastward propagation, Geophys. Res. Lett., 47, e2020GL087788, https://doi.org/10.1029/2020GL087788, 2020b.

Liang, Y.; Du, Y.; Zhang, L.; Zheng, X.; Qiu, S. The 30–50-Day Intraseasonal Oscillation of SST and Precipitation in the South Tropical Indian Ocean, Atmos., 9, 69. https://doi.org/10.3390/atmos9020069, 2018.

Liang, Y., and Du, Y.: Oceanic impacts on 50–80-day intraseasonal oscillation in the eastern tropical Indian Ocean, Clim. Dynam., 59, 1283–1296, https://doi.org/10.1007/s00382-021-06041-y, 2022.

Liebmann, B.: Description of a complete (interpolated) outgoing longwave radiation dataset, B. Am. Meteorol. Soc., 77, 1275–1277, 1996.

Madden, R. A., and Julian, P. R.: Description of global-scale circulation cells in the tropics with a 40-50 day period, J. Atmos. Sci., 29, 1109-1123, https://doi.org/10.1175/1520-0469(1972)029<1109:DOGSCC>2.0.CO;2, 1972.

Maloney, E., and Sobel, A. H.: Surface fluxes and ocean coupling in the tropical intraseasonal oscillation. J. Climate, 17, 4368–4386, https://doi.org/10.1175/JCLI-3212.1, 2004.

Newman, M., Sardeshmukh, P. D., and Penland, C.: How important is air–sea coupling in ENSO and MJO evolution? J. Climate, 22, 2958– 2977, https://doi.org/10.1175/2008JCLI2659.1, 2009.

Pariyar, S.K., Keenlyside, N., Tseng, W.-L., Hsu, H.-H., and Tsuang, B.-J. The role of air–sea coupling on November–April intraseasonal rainfall variability over the South Pacific, Clim. Dynam., 60, 1121–1136, https://doi.org/10.1007/s00382-022-06354-6, 2023.

已下移 [17]: Tsuang, B.-J., Tu, C.-Y.,

已設定格式: 圖樣:清除 (白色)

已下移 [18]: .-L.,

已上移 [16]: .-I.:

已刪除: Wu, T.-Y., Chen, Y

已刪除: and Hsieh, C

已刪除: Observation and Simulation of Meteorology and Surface Energy Components over the South China Sea in Summers of 2004 and 2006, Terr. Atmos. Ocean. Sci., 21, 325–342, https://doi.org/ 10.3319/TAO.2009.04.07.01(A), 2010.
Lan, Y.-Y.,

格式化: 左右對齊

Pei, S., Shinoda, T., Soloviev, A., and Lien, R.-C.: Upper ocean response to the atmospheric cold pools associated with the Madden-Julian Oscillation, Geophys. Res. Lett., 45, 5020–5029, https://doi.org/10.1029/2018GL077825, 2018.

Rasch, P. J., Xie, S., Ma, P.-L., Lin, W., Wang, H., Tang, Q., Bur- rows, S. M., Caldwell, P., Zhang, K., Easter, R. C., Cameron- Smith, P., Singh, B., Wan, H., Golaz, J.-C., Harrop, B. E., Roesler, E., Bacmeister, J., Larson, V. E., Evans, K. J., Qian, Y., Taylor, M., Leung, L. R., Zhang, Y., Brent, L., Branstet- ter, M., Hannay, C., Mahajan, S., Mametjanov, A., Neale, R., Richter, J. H., Yoon, J.-H., Zender, C. S., Bader, D., Flan- ner, M., Foucar, J. G., Jacob, R., Keen, N., Klein, S. A., Liu, X., Salinger, A. G., Shrivastava, M., and Yang, Y.: An overview of the atmospheric component of the Energy Exascale Earth System Model, J. Adv. Model Earth Sy., 11, 2377–2411, https://doi.org/10.1029/2019ms001629, 2019.

Rayner, N. A., Parker, D. E., Horton, E. B., Folland, C. K., Alexander, L. V., Rowell, D. P., Kent, E. C., and Kaplan, A.: Global analyses of sea surface temperature, sea ice, and night marine air temperature since the late nineteenth century, J. Geophys. Res., 108(D14), 4407, https://doi.org/10.1029/2002JD002670, 2003.

Ren, P. F., Gao, L., Ren, H.-L., Rong, X., and Li, J.: Representation of the Madden–Julian Oscillation in CAMSCSM, J. Meteor. Res., 33, 627–650, https://doi.org/10.1007/s13351-019-8118-x, 2019.

Savarin, A., and Chen, S. S.: Pathways to better prediction of the MJO: 2. Impacts of atmosphere-ocean coupling on the upper ocean and MJO propagation, J. Adv. Model. Earth Syst., 14, e2021MS002929, https://doi.org/10.1029/2021MS002929, 2022.

Shinoda, T., Pei, S., Wang, W., Fu, J. X., Lien, R.-C., Seo, H., and Soloviev, A.: Climate process team: Improvement of ocean component of NOAA climate forecast system relevant to Madden-Julian Oscillation simulations, J. Adv. Model. Earth Syst., 13(12), e2021MS002658. https://doi.org/10.1029/2021MS002658, 2021.

Seo, H., Subramanian, A. C., Miller, A. J., and Cavanaugh, N. R.: Coupled impacts of the diurnal cycle of sea surface temperature on the Madden–Julian oscillation, J. Climate, 27(22), 8422– 8443. https://doi.org/10.1175/JCLI-D-14-00141.1, 2014.

Sobel, A. H., and Gildor, H.: A simple time-dependent model of SST hot spots. J. Climate, 16, 3978–3992, https://doi.org/10.1175/1520-0442(2003)016<3978:ASTMOS>2.0.CO;2, 2003.

Sobel, A. H., Maloney, E. D., Bellon, G., and Frierson, D. M.: Surface Fluxes and Tropical Intraseasonal Variability: a Reassessment, J. Adv. Model. Earth Syst., 2, 2, https://doi.org/10.3894/JAMES.2010.2.2, 2010.

已移動 (插入) [18]

格式化: 左右對齊

已上移 [15]: Geophys. Res

已下移 [20]: Seo, H., Subramanian, A. C., Miller, A. J., and Cavanaugh, N. R.: Coupled impacts of the diurnal cycle of sea surface temperature on the Madden–Julian oscillation, J. Climate, 27(22), 8422– 8443. https://doi.org/10.1175/JCLI-D-14-00141.1, 2014.

已刪除: Sentić, S., Fuchs-Stone, Ž., and Raymond, D. J.: TheMadden-Julian Oscillation and meaneasterly winds, J.

已設定格式: 圖樣:清除 (白色)

已刪除: .-Atmos., 125,e2019JD030869. https://doi.org/10.1029/2019JD030869, 2020.

已下移 [19]: Sobel, A., Wang, S., and Kim, D.: Moist static energy budget of the MJO during DYNAMO, J. Atmos. Sci., 71(11), 4276– 4291, https://doi.org/10.1175/JAS-D-14-0052.1, 2014.

已設定格式: 圖樣:清除

已移動 (插入) [20]

已移動 (插入) [10]

Sobel, A., Wang, S., and Kim, D.: Moist static energy budget of the MJO during DYNAMO, J. Atmos. Sci., 71(11), 4276– 4291, https://doi.org/10.1175/JAS-D-14-0052.1, 2014.

Stan, C.: The role of SST variability in the simulation of the MJO, Clim. Dynam., 51, 2943–2964, https://doi.org/10.1007/s00382-017-4058-2, 2018.

Tseng, W.-L., Tsuang, B.-J., Keenlyside, N. S., Hsu, H.-H. and Tu, C.-Y.: Resolving the upper-ocean warm layer improves the simulation of the Madden-Julian oscillation, Clim. Dynam., 44, 1487–1503, https://doi.org/10.1007/s00382-014-2315-1, 2015.

Tseng, W.-L., Hsu, H.-H., Keenlyside, N., Chang, C.-W. J., Tsuang, B.-J., Tu, C.-Y., and Jiang, L.-C.: Effects of Orography and Land–Sea Contrast on the Madden–Julian Oscillation in the Maritime Continent: A Numerical Study Using ECHAM-SIT, J. Climate, 30, 9725–9741, https://doi.org/10.1175/JCLI-D-17-0051.1, 2017.

Tseng, W.-L., Hsu, H.-H., Lan, Y.-Y., Lee, W.-L., Tu, C.-Y., Kuo, P.-H., Tsuang, B.-J., and Liang, H.-C.: Improving Madden–Julian oscillation simulation in atmospheric general circulation models by coupling with a one-dimensional snow–ice–thermocline ocean model, Geosci. Model Dev., 15, 5529–5546, https://doi.org/10.5194/gmd-15-5529-2022, 2022.

Tulich, S. N., and Kiladis, G. N.: On the Regionality of moist kelvin waves and the MJO: The critical role of the background zonal flow, J. Adv. Model. Earth Syst., 13(9), e2021MS002528. https://doi.org/10.1029/2021MS002528, 2021.

Voldoire, A., Roehrig, R., Giordani, H., Waldman, R., Zhang, Y., Xie, S., and Bouin, M.-N.: Assessment of the sea surface temperature diurnal cycle in CNRM-CM6-1 based on its 1D coupled configuration, Geosci. Model Dev., 15, 3347–3370, https://doi.org/10.5194/gmd-15-3347-2022, 2022.

Wang, W., Hung, M.-P., Weaver, S. J., Kumar, A., and Fu, X.: MJO prediction in the NCEP Climate Forecast System version 2, Clim. Dynam., 42, 2509–2520, https://doi.org/10.1007/s00382-013-1806-9, 2014.

Wang, L. and Li, T.: Effect of vertical moist static energy advection on MJO eastward propagation: Sensitivity to analysis domain, Clim. Dynam., 54, 2029–2039, https://doi.org/10.1007/s00382-019-05101-8, 2020.

Watterson, I. G.: The sensitivity of subannual and intraseasonal tropical variability to model ocean mixed layer depth, J. Geophys. Res., 107, 4020, https://doi.org/10.1029/2001JD000671, 2002.

Wheeler, M. C., and Hendon, H. H.: An all-season real-time multivariate MJO index: development of an index for monitoring and prediction, Mon. Weather Rev., 132, 1917–1932, https://doi.org/10.1175/1520-

已移動 (插入) [19]

格式化: 左右對齊

已移動 (插入) [17]

已設定格式: 圖樣:清除

格式化: 左右對齊

已設定格式: 圖樣:清除 (白色)

格式化: 左右對齊

已上移 [13]: B.,

已設定格式: 圖樣:清除 (自訂色彩(RGB(252,252,252)))

已刪除: Liu, F., and Chen, G.: A trio-interaction theory for Madden–Julian oscillation, Geosci

已上移 [12]: . Lett.,

已設定格式: 圖樣:清除 (白色)

已刪除: 3(1), 1-16. https://doi.org/10.1186/s40562-016-0066-z, 2016.
Wang,

已設定格式: 圖樣:清除

格式化: 左右對齊

0493(2004)132<1917:AARMMI>2.0.CO;2, 2004.

Wheeler, M., and Kiladis, G. N.: Convectively coupled equatorial waves: Analysis of clouds and temperature in the wavenumber-frequency domain, J. Atmos. Sci., 56, 374– 399, https://doi.org/10.1175/1520-0469(1999)056<0374:CCEWAO>2.0.CO;2, 1999.

Wu, C.-H., and Hsu, H.-H.: Potential Influence of Topography on the MJO in the Maritime Continent, J. Climate, 22, 5433-5448, https://doi.org/10.1175/2009JCLI2825.1, 1999.

Wu, J., Li, Y., Luo, J.-J. and Jiang, X.: Assessing the role of air–sea coupling in predicting Madden–Julian oscillation with an Atmosphere–Ocean coupled model, J. Clim. 34 9647–63, https://doi.org/10.1175/JCLI-D-20-0989.1, 2021.

Zhang, L., and Han, W.: Barrier for the eastward propagation of Madden–Julian Oscillation over the maritime continent: A possible new mechanism, Geophys. Res. Lett., 47(21), e2020GL090211. https://doi.org/10.1029/2020gl090211, 2020.

Zhao, N., and Nasuno, T.: How Does the Air–Sea Coupling Frequency Affect Convection During the MJO Passage?, J. Adv. Model. Earth Sy., 12, e2020MS002058, https://doi.org/10.1029/2020MS002058, 2020.

已刪除: R. G
已設定格式: 字型色彩: 自動
已刪除: Kirtman, B. P.: Roles
已刪除: Indian and Pacific Ocean air–sea coupling
已設定格式: 字型色彩: 自動
已設定格式: 字型色彩: 自動
已刪除: tropical atmospheric variability, Clim. Dynam., 25, 155–170
已設定格式: 字型色彩: 自動
已設定格式: 字型色彩: 自動
已設定格式: 字型色彩: 自動, 圖樣:清除
已設定格式: 字型色彩: 自動
已刪除: 1007/s00382-005-0003-x, 2005
已設定格式: 字型色彩: 自動
已移動 (插入) [14]
已設定格式: 預設段落字型, 字型色彩: 自動, 圖樣:清除
格式化: 左右對齊

Table 1. Two sets of experiments with different SST feedback frequencies: high-frequency (C–CTL, C–1day and C–3days) and low-frequency (C–6days, C–12days, C–18days, C–24days and C–30days).

subseasonal sets	**high-frequency SST (< 6 days)**			**low-frequency SST (6-30 days)**				
experiments	C–CTL	C–1day	C–3days	C–6days	C–12days	C–18days	C–24days	C–30days
atmosphere to ocean frequency	48/1day							
ocean to atmosphere Frequency	48/1day	1/1day	1/3days	1/6days	1/12days	1/18days	1/24days	1/30days

已刪除: marine feedback frequency
已刪除: SST feedback
已刪除: SST feedback
已刪除:) under SST sub-seasonal variability.
格式化表格
插入儲存格
已設定格式: 字型: 10 點
已設定格式: 字型: 10 點
格式化: 左右對齊
格式化: 左右對齊
已設定格式: 字型: 10 點
已設定格式: 字型: 10 點
格式化: 左右對齊
格式化: 左右對齊
格式化: 左右對齊
格式化表格
已設定格式: 字型: 10 點
已刪除: day
已設定格式: 字型: 10 點
格式化: 左右對齊
插入儲存格
已設定格式: 字型: 10 點
已設定格式: 字型: 10 點
已設定格式: 字型: 10 點
格式化: 左右對齊
已設定格式: 字型: 10 點
格式化: 左右對齊
已設定格式: 字型: 10 點
格式化: 左右對齊
已刪除: day
已設定格式: 字型: 10 點
已設定格式: 字型: 10 點
已設定格式: 字型: 10 點
格式化: 左右對齊
已設定格式: 字型: 10 點
格式化: 左右對齊
已設定格式: 字型: 10 點
格式化: 左右對齊
格式化: 左右對齊
格式化: 左右對齊
已刪除:

Table 2. Key intraseasonal (20–100-day bandpass filtered) ocean temperatures in all experiments: SST, differences between SST and temperatures at 10m depth ($\overline{\Delta T}_{0-10m}$) and 30m depth ($\overline{\Delta T}_{0-30m}$), t max/mini SST and 10m-depth temperature (T_{10m}) in the area of (110–130° E, 5–15° S) during a MJO cycle for the observation (OISST), AGCM (A–CTL), high-frequency experiments (C–CTL, C–1day, and C–3days), and low-frequency experiments (C–6days, C–12days, C–18days, C–24days, and C–30days)

(110–130° E, 5–15° S)		obs.	AGCM	high-frequency			low-frequency				
experiments		OI SST[1]	A–CTL[2]	C–CTL	C–1day	C–3days	C–6days	C–12days	C–18days	C–24days	C–30days
DJF seasonal mean	SST	302.2 ±0.96	302.2 ±0.77	300.8 ±0.76	301.2 ±0.76	301.2 ±0.75	301.2 ±0.75	301.4 ±0.75	301.6 ±0.80	302.0 ±1.06	302.7 ±1.71
	$\overline{\Delta T}_{0-10m}$	-	-	0.1 ± 0.22	0.1 ± 0.22	0.1 ± 0.21	0.1 ± 0.23	0.2 ± 0.25	0.3 ± 0.32	0.5 ± 0.50	1.0 ± 0.95
	$\overline{\Delta T}_{0-30m}$	-	-	0.8 ± 0.79	0.7 ± 0.70	0.6 ± 0.69	0.8 ± 0.70	0.8 ± 0.70	1.0 ± 0.73	1.4 ± 0.96	2.1 ± 1.54
phase's mean in boreal winter	max SST (phase)	0.21 (ph2)	0.02 (ph2)	0.24 (ph3)	0.26 (ph3)	0.22 (ph3)	0.32 (ph3)	0.36 (ph3)	0.43 (ph3)	0.50 (ph3)	0.62 (ph2)
	max T_{10m} (phase)	-	-	0.15 (ph4)	0.17 (ph4)	0.14 (ph3)	0.19 (ph3)	0.21 (ph3)	0.26 (ph3)	0.30 (ph3)	0.35 (ph2)
	mini SST (phase)	-0.21 (ph7)	-0.003 (ph8)	-0.17 (ph7)	-0.22 (ph7)	-0.19 (ph7)	-0.25 (ph7)	-0.28 (ph7)	-0.38 (ph7)	-0.52 (ph6)	-0.60 (ph6)
	mini T_{10m} (phase)	-	-	-0.11 (ph8)	-0.12 (ph7)	-0.11 (ph8)	-0.15 (ph7)	-0.17 (ph7)	-0.24 (ph7)	-0.33 (ph6)	-0.33 (ph6)

Note: [1]daily average data, [2] monthly average data.

已刪除: The average DJF temperature difference
已刪除:
已刪除: and the boreal winter phase mean of 20–100-day
已刪除:), with
已刪除:)
已設定格式
已設定格式
已設定格式
已設定格式
已設定格式
已設定格式
插入儲存格
已設定格式
已設定格式
格式化
已設定格式
格式化
已設定格式
格式化
已設定格式
已設定格式
已設定格式
格式化
已設定格式
格式化
已設定格式
格式化
已設定格式
已設定格式
已設定格式
格式化
已設定格式
已設定格式
已設定格式
格式化
已設定格式
格式化
已設定格式
格式化
格式化
已設定格式
格式化
格式化
已設定格式
已設定格式
格式化
已設定格式
格式化
已設定格式
格式化
格式化
插入儲存格
格式化
已設定格式
已設定格式

Figure List

Figure 1. Wavenumber–frequency spectra for 850-hPa zonal wind averaged over 10° S–10° N in boreal winter after removing the climatological mean seasonal cycle. Vertical dashed lines represent periods at 80 and 30 days. (a)–(j) are from ERA5 reanalysis, A–CTL, C–CTL, C–1day, C–3days, C–6days, C–12days, C–18days, C–24days, and C–30days, respectively.

Figure 2. Hovmöller diagrams of correlation between precipitation averaged over 10° S–5° N, 75–100° E and precipitation (color) and 850-hPa zonal wind (contour) averaged over 10° N–10° S. (a)–(j) are arranged in the same order as in Fig. 1 for GPCP/ERA5 and all experiments. All data are 20–100-day bandpass filtered.

Figure 3. Zonal wavenumber–frequency power spectra of anomalous OLR (colors) and phase lag with U850 (vectors) for the symmetric component of tropical waves, with the vertically upward vector representing a phase lag of 0° and phase lag increasing clockwise. Three dispersion straight lines with increasing slopes representing the equatorial Kelvin waves (derived from the shallow water equations) corresponding to three equivalent depths, 12, 25, and 50 m, respectively. (a)–(j) are arranged in the same order as in Fig. 1 for NOAA/ERA5 and all experiments.

Figure 4. Phase-longitude Hovmöller diagrams of 20–100-day filtered precipitation (mm day^{-1}, shaded) and SST anomaly (K, contour) averaged over 10° N–10° S from phase 1 to 8. Contour interval is 0.03; solid, dashed, and thick-black lines represent positive, negative, and zero values, respectively. (a)–(j) are arranged in the same order as in Fig. 1 for NOAA/ERA5 and all experiments.

Figure 5. Phase-vertical Hovmöller diagrams of 20–100-day specific humidity (shading, g kg^{-1}) and air temperature (contoured, K) averaged over 5–20° S, 120–150° E; solid, dashed, and thick-black curves are positive, negative, and zero values, respectively. (a)–(j) are arranged in the same order as in Fig. 1 for NOAA/ERA5 and all experiments.

Figure 6. The 20–100-day filtered oceanic temperature (K, shaded and contour, interval 0.03) at phase 2–3 (Left column) and phase 4–5 (Right column) averaged over 0–15° S between 0 and 60 m depth. (a)–(b) are from C–CTL, (c)–(d) are from C–1day, (e)–(f) are from C–3days, (g)–(h) are from C–6days, (i)–(j) are from C–12days, (k)–(l) are from C–18days, (m)–(n) are from C–24days, and (o)–(p) are from C–30days.

已刪除: , respectively.
已刪除: i
已刪除: the
已刪除: the
已刪除: the intraseasonally filtered
已刪除: i) arrange
已刪除: are same
已刪除: from

Figure 7. The lead–lag relationship between MJO-related atmosphere and SST variation from phase 1 to 8 averaged within 110–130° E and 5–15° S. The variables analyzed include 20-100-day filtered LHF, green shading), OLR (yellow bar chart), FSNS, (orange bar chart), U850 (purple bar chart), 30-m T (multiplied by 100, black line), and SST (multiplied by 10, orange line). Variables denoted with L (R) are scaled by the left (right) y-axis. (a)–(j) are from ERA5/OISST reanalysis, A–CTL, C–CTL, C–1day, C–3days, C–6days, C–12days, C–18days, C–24days, and C–30days, respectively.

Figure 8. Averaged 20–100-day filtered fields at phase 2–3. (Upper row) OLR (W m^{-2}, shaded) and 200 hPa zonal and meridional wind anomaly (m s^{-1}, vector with reference vector shown at the top right corner, latent heat flux (W m^{-2}, shaded, positive representing upward), and 10-m wind anomaly (m s^{-1}, contour interval 0.5). (Second row) net surface heat flux (W m^{-2}, shaded) and net solar radiation (W m^{-2}, contour interval 6). (Third row) SST (K, shaded) and 850 hPa zonal and meridional wind anomaly (m s^{-1}, vector with reference vector shown at the top right corner. The number of days used to generate the composite is shown at the bottom right corner. (a), (d), (g) and (j) are from C–18days; (b), (e), (h) and (k) are from C–24days, and (c), (f), (i) and (l) are from C–30days, respectively. Solid, dashed, and thick-black lines represent positive, negative, and zero values, respectively.

Figure 9. Averaged 20–100-day filtered column-integrated MSE budget terms (J kg^{-1} s^{-1}) in 10° S–0° N/S, 120–150° E for ERA5 and all model simulations. Colors represent different datasets: green for REA5, light gray for A–CTL, red, orange and wathet blue for high-frequency experiments (C–CTL, C–1day, and C–3days, respectively), purple, black, dark brown, dark green, and dark gray for low-frequency experiments (C–6days, C–12days, C–18days, C–24days, and C–30days, respectively). The bars from left to right represent MSE tendency (<dmdt>), vertical MSE advection (-<wdmdp>), horizontal MSE advection (-<vdm>), surface latent heat flux (LH), surface sensible heat flux (SH), shortwave radiation flux (<SW>), longwave radiation flux (<LW>), and residual terms.

Figure 10. Filtered the column-integrated MSE tendency (J kg^{-1} s^{-1}, shading), precipitation (mm d^{-1}, contours interval 1.5) and 850-hPa wind (green vector, reference vector 2 m s^{-1}) in phase 5: (a) ERA5, (b) A−CTL, (c) C−CTL, (d) C−1day, (e) C−3days, (f) C−6days, (g) C−12days, (h) C−18days, (i) C−24days, and (i) C−30days. Solid-red, dashed-blue, and thick-black curves represent positive, negative, and zero values, respectively.

已移動 (插入) [21]

格式化: 左右對齊

Figure 11. The projection of each MSE component onto the ERA5 column-integrated MSE tendency at phase 5 over the MC (20° S–20° N, 90–210° E): <dmdt>, -<wdmdp>, -<vdm>, Qr, Fs, and residual; decomposition of horizontal MSE advection to zonal and meridional advection (-<udmdt> and -<vdmdy>).

Figure 12. Filtered column-integrated vertical (J kg^{-1} s^{-1}, shading) and horizontal MSE advection (J kg^{-1} s^{-1}, contours interval 6.0), and 200-hPa wind (green vector with reference vector 3 m s^{-1}): (a) ERA5, (b) A−CTL, (c) C−CTL, (d) C−1day, (e) C−3days, (f) C−6days, (g) C−12days, (h) C−18days, (i) C−24days, and (j) C−30days. Solid-blue, dashed-red, and thick-black curves represent positive, negative, and zero values, respectively.

Figure 13. Schematic diagrams illustrate the anomalous circulation and moistening processes during the eastward propagation of the MJO in experiments: (a) A−CTL, (b) high-frequency SST feedback experiments (C−CTL, C−1day, and C−3days), (c) low-frequency SST feedback experiments (C−6days, C−12days, and C−18days), and (d) C−24days and C−30days experiment. In each panel, the horizontal line represents the equator. The size of clustering gray clouds indicates the strength of convective organization. A red ellipse indicates convection-driven circulation. In the coupled simulations, light red (blue) filled ovals represent warm (cold) SST anomalies, respectively, and grass green filled rectangle represent latent heat flux. Unresolved convective processes are indicated by black dots representing low-level moisture convergence. Low-level moisture convergence into the equatorial trough is shown by light blue arrows, while midlevel moisture advection is represented by left-pointing green arrows. The deeper colors or thicker lines on the map indicate stronger anomalies of the MJO perturbations. Note: The concept of the figure is based on DeMott et al. (2014).

已移動 (插入) [22]
格式化: 左右對齊
已移動 (插入) [23]
格式化: 左右對齊
已移動 (插入) [24]

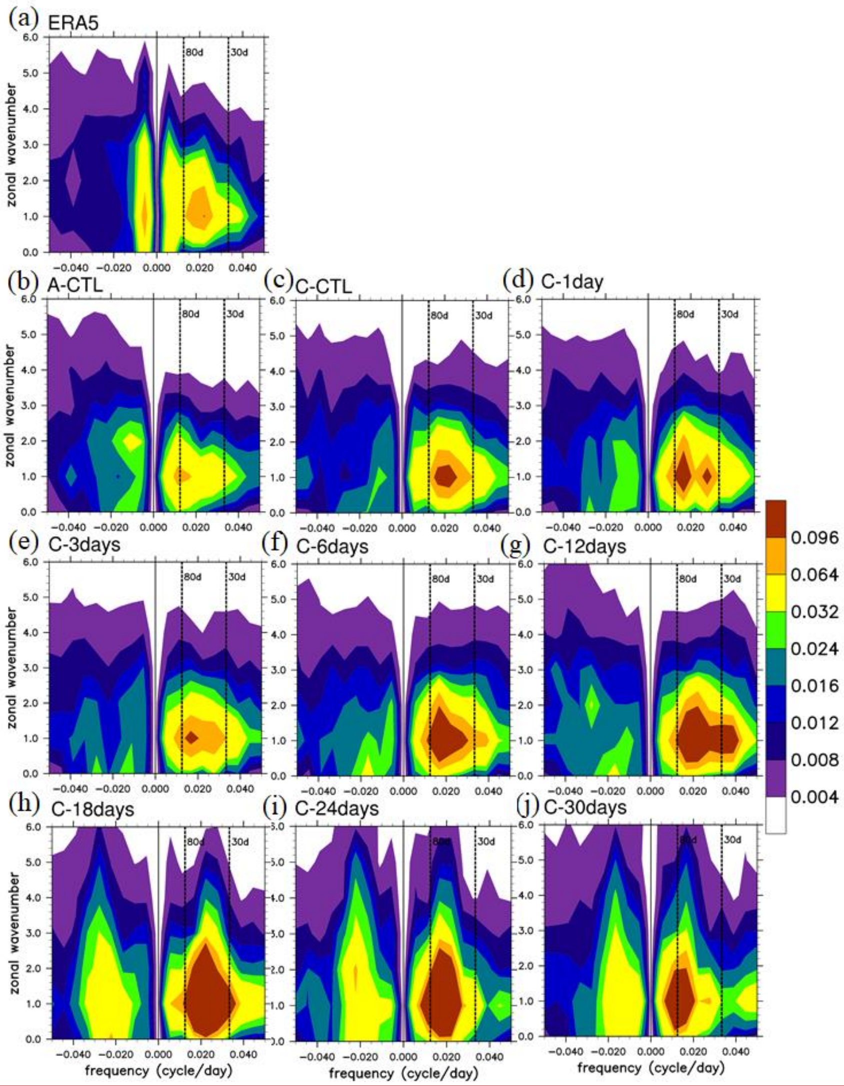

Figure 1. Wavenumber–frequency spectra for 850-hPa zonal wind averaged over 10° S–10° N in boreal winter after removing the climatological mean seasonal cycle. Vertical dashed lines represent periods at 80 and 30 days. (a)–(j) are from ERA5 reanalysis, A–CTL, C–CTL, C–1day, C–3days, C–6days, C–12days, C–18days, C–24days, and C–30days, respectively.

已移動 (插入) [25]

格式化: 格線被設定時，不要調整右側縮排, 沒有段落遺留字串控制, 不調整中文字與英文字間的距離, 不調整中文字與數字間的距離

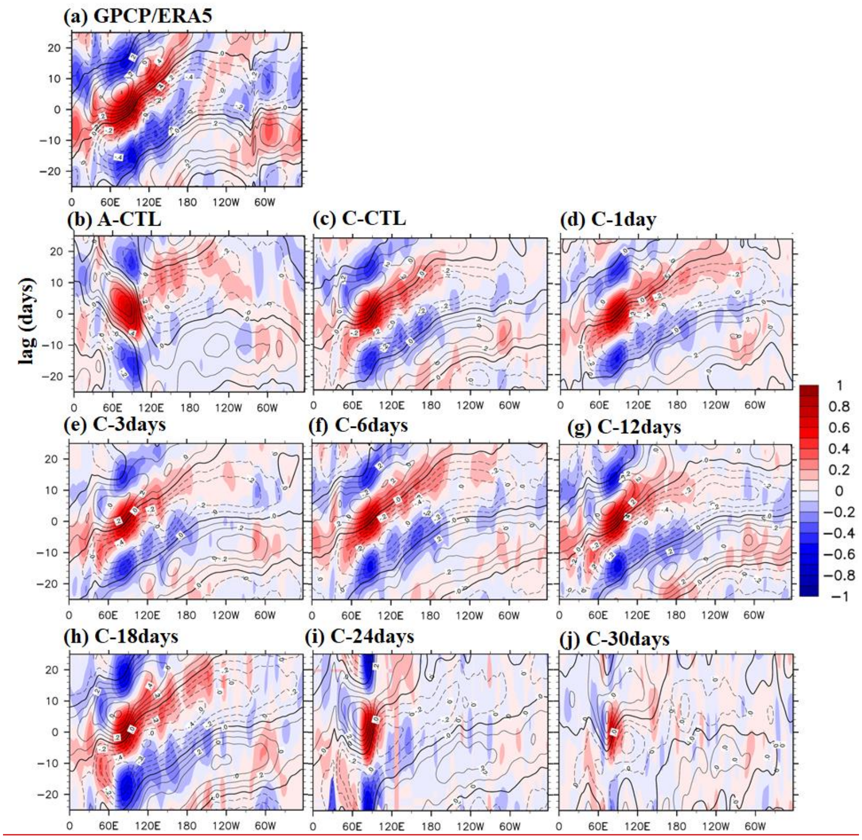

Figure 2. Hovmöller diagrams of correlation between precipitation averaged over 10° S–5° N, 75–100° E and precipitation (color) and 850-hPa zonal wind (contour) averaged over 10° N–10° S. (a)–(j) are arranged in the same order as in Fig. 1 for GPCP/ERA5 and all experiments. All data are 20–100-day bandpass filtered.

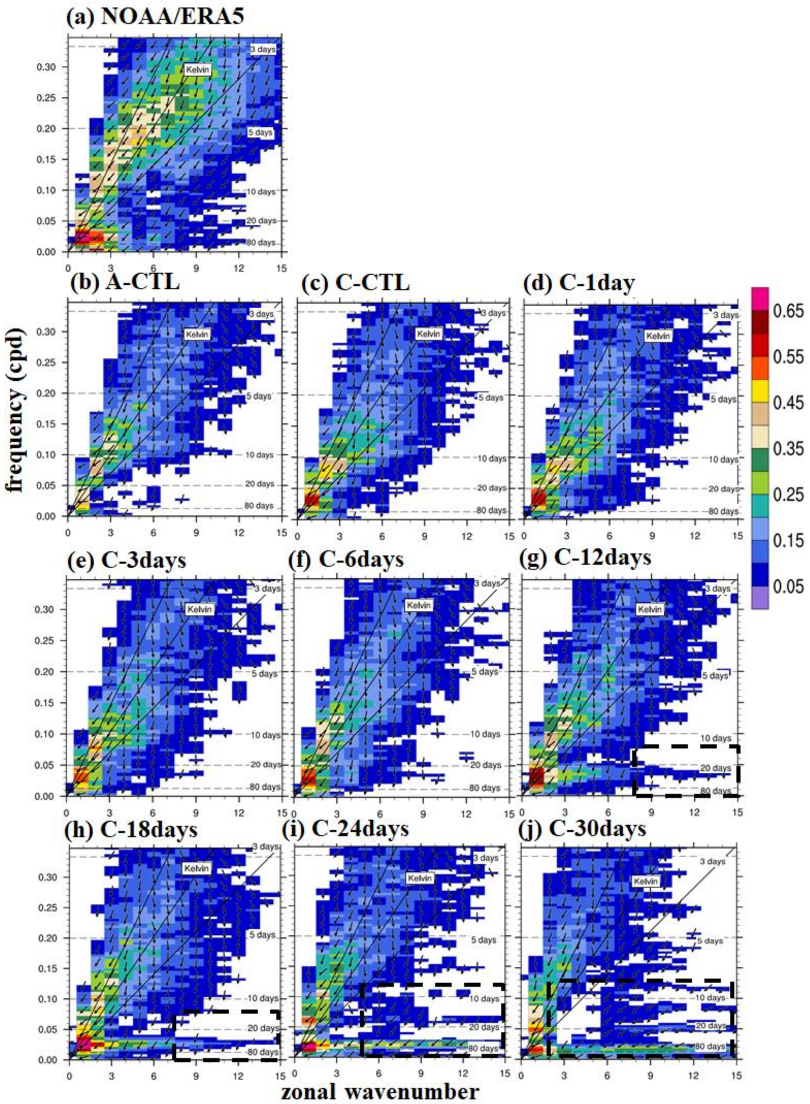

Figure 3. Zonal wavenumber–frequency power spectra of anomalous OLR (colors) and phase lag with U850 (vectors) for the symmetric component of tropical waves, with the vertically upward vector representing a phase lag of 0° with phase lag increasing clockwise. Three dispersion straight lines with increasing slopes represent the equatorial Kelvin waves (derived from the shallow water equations) corresponding to three equivalent depths, 12, 25, and 50 m, respectively. (a)–(j) arrange in order are same order as in Fig. 1 for NOAA/ERA5 and all experiments.

已設定格式
格式化: 左右對齊
已刪除: i
已刪除: from
已設定格式

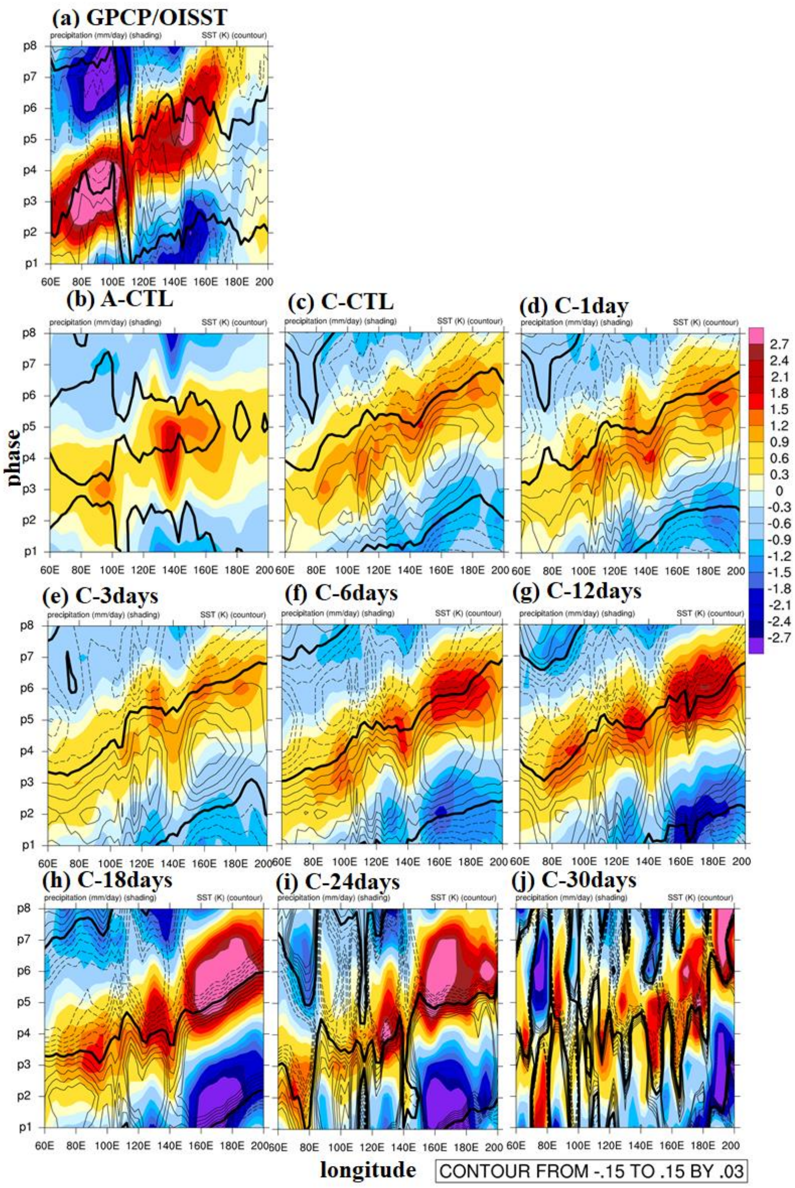

Figure 4. Phase-longitude Hovmöller diagrams of 20–100-day filtered precipitation (mm day^{-1}, shaded) and SST anomaly (K, contour) averaged over 10° N–10° S from phase 1 to 8. Contour interval is 0.03; solid, dashed, and thick-black lines represent positive, negative, and zero values, respectively. (a)–(j) are arranged in the same order as in Fig. 1 for NOAA/ERA5 and all experiments.

已刪除:
Figure 4. Phase-longitude Hovmöller diagrams of 20–100-day filtered precipitation (mm day^{-1}, shaded) and SST anomaly (K, contour) averaged over 10° N–10° S from phase 1 to 8. Contour interval is 0.03; solid, dashed, and thick-black lines represent positive, negative, and zero values, respectively. (a)–(i) arrange in order are same as Fig. 1 from GPCP/OISST and all experiments.

Figure 5. Phase-vertical Hovmöller diagrams of 20–100-day specific humidity (shading, g kg^{-1}) and air temperture ...

已上移 [21]: **Figure**

已上移 [22]: **Figure**

已上移 [23]: **Figure**

已上移 [24]: Low-level moisture convergence into the equatorial trough is shown by light blue arrows, while

已上移 [25]: **Figure 1.** Wavenumber–frequency spectra for 850-hPa zonal wind averaged over 10° S–10° N in boreal

已刪除: **9.** The lead-lag relationship between MJO-related atmosphere and sub-seasonal SST variation is examined ...

已刪除: **11.** The bar chart illustrates anomalies in the average 20–100-day filtered column-integrated MSE budget terms ...

已刪除: **12.** Phase 5 anomalies of 20–100-day filtered the column-integrated MSE tendency (J kg^{-1} s^{-1}, shading), ...

已刪除: factors. Note: The concept of the figure is based on DeMott et al. (2014), as depicted in Fig. 11. ...

已刪除: , respectively. (a)–(i) are from ERA5 reanalysis, A–CTL, C–CTL, C–1day, C–3days, C–6days, C–12days, C– ...

已刪除: i) arrange

已刪除: are same

已刪除: from GPCP/OISST

已設定格式

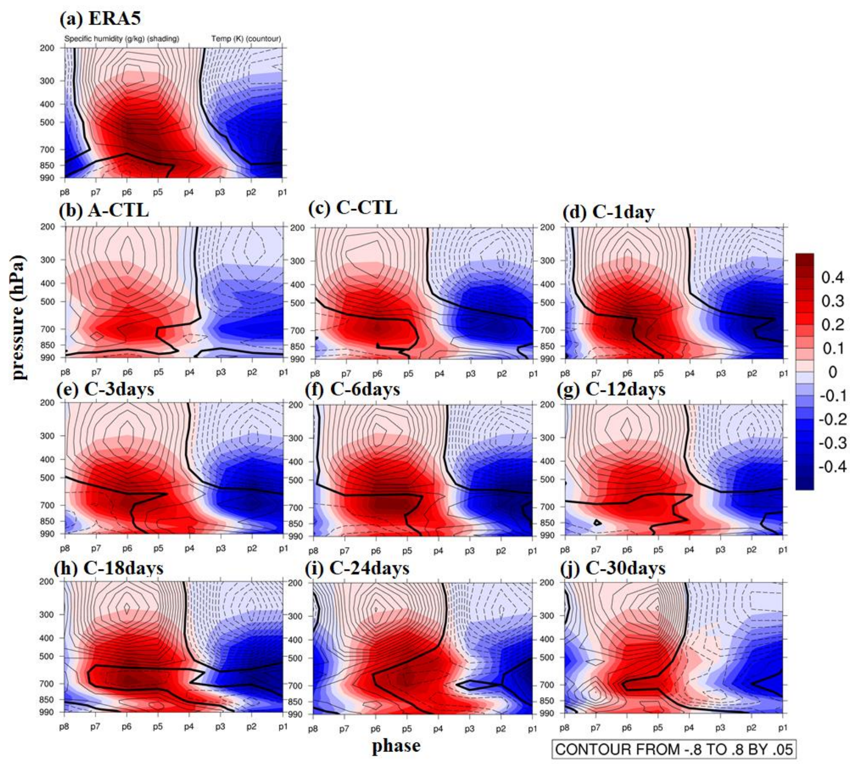

Figure 5. Phase-vertical Hovmöller diagrams of 20–100-day specific humidity (shading, g kg−1) and air temperature (contoured, K) averaged over 5–20° S, 120–150° E; solid, dashed, and thick-black curves are positive, negative, and zero values, respectively. (a)–(j) are arranged in the same order as in Fig. 1 for NOAA/ERA5 and all experiments.

已刪除: 分頁符號

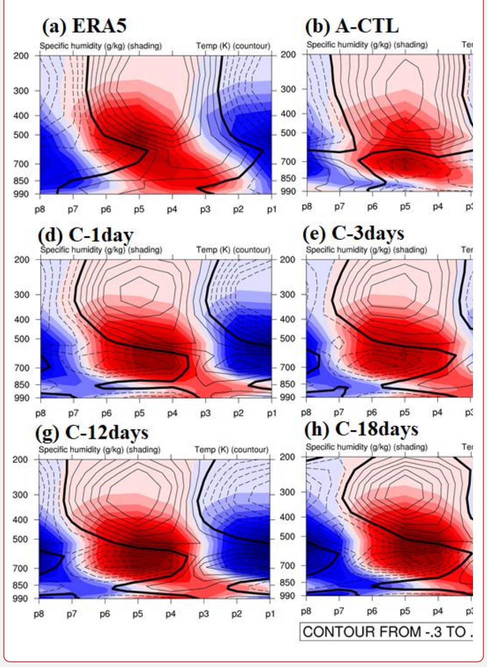

已設定格式: 非加寬 / 緊縮 , 調整字距 18 點

格式化: 左右對齊

已設定格式: 調整字距 18 點

已刪除: 10° N–10

已設定格式: 非上標/ 下標, 調整字距 18 點

已設定格式: 調整字距 18 點

已設定格式: 調整字距 18 點

已刪除: temperture

已設定格式: 調整字距 18 點

已刪除: i) arrange

已設定格式: 調整字距 18 點

已設定格式: 調整字距 18 點

已刪除: are same

已設定格式: 調整字距 18 點

已刪除: from

已設定格式: 調整字距 18 點

已設定格式: 調整字距 18 點

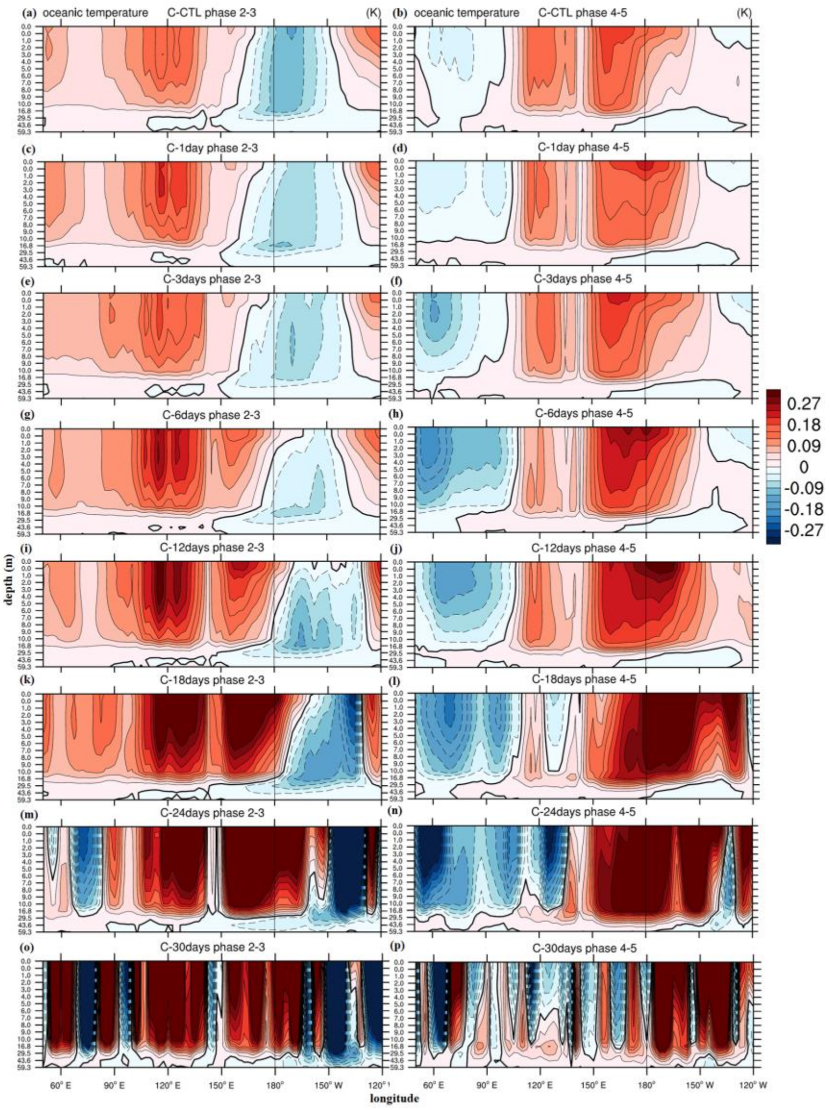

Figure 6. The 20–100-day filtered oceanic temperature (K, shaded and contour, interval 0.03) at phase 2–3 (Left column) and phase 4–5 (Right column) averaged over 0–15° S between 0 and 60 m depth. (a)–(b) are from C–CTL, (c)–(d) are from C–1day, (e)–(f) are from C–3days, (g)–(h) are from C–6days, (i)–(j) are from C–12days, (k)–(l) are from C–18days, (m)–(n) are from C–24days, and (o)–(p) are from C–30days.

已刪除:

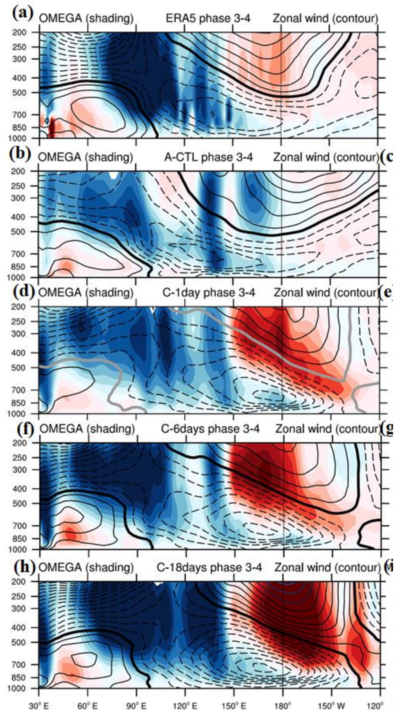

已刪除: 15° N–15° S averaged p-vertical velocity anomaly (Pa s^{-1}, shaded) and zonal wind anomaly (m s^{-1}, contour, interval 0.5) between phase 3 and phase 4; solid, dashed, and thick-black lines represent positive, negative, and zero values, respectively.

分頁符號

已刪除: average

已設定格式: 字型: 粗體

格式化: 左右對齊

已設定格式: 字型: 粗體

已刪除: for MJO phase 2–3. (

已刪除: g

已刪除: , respectively

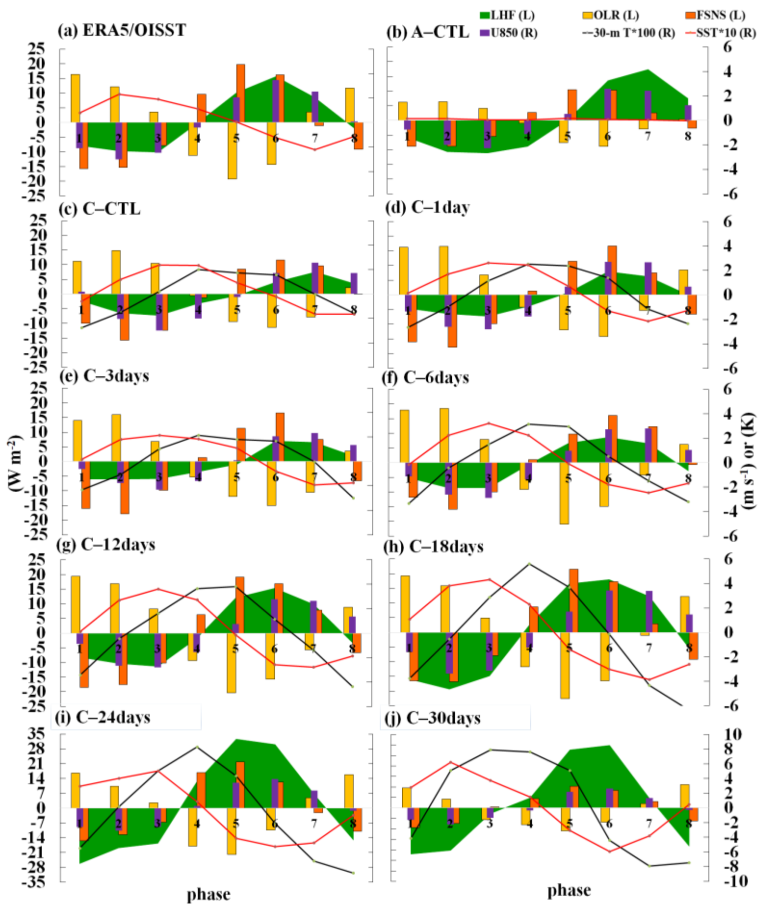

Figure 7. The lead–lag relationship between MJO-related atmosphere and SST variation from phase 1 to 8 averaged within 110–130° E and 5–15° S. The variables analyzed include 20-100-day filtered LHF, green shading), OLR (yellow bar chart), FSNS, (orange bar chart), U850 (purple bar chart), 30-m T (multiplied by 100, black line), and SST (multiplied by 10, orange line). Variables denoted with L (R) are scaled by the left (right) y-axis. (a)–(j) are from ERA5/OISST reanalysis, A–CTL, C–CTL, C–1day, C–3days, C–6days, C–12days, C–18days, C–24days, and C–30days, respectively.

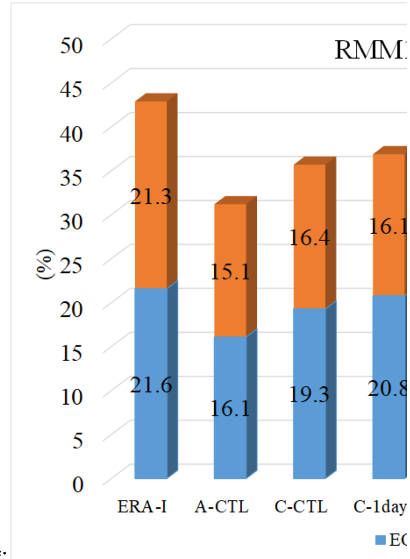

已刪除:

Figure 8. The near-equatorial RMM1 and RMM2 variances in a bar graph based on Wheeler and Hendon (2004) with observation and reanalysis data (NOAA/ERA5), AGCM (A–CTL), high-frequency experiments (C–CTL, C–1day and C–3days) and low-frequency experiments (C–6days, C–12days, C–18days and C–30days).

分頁符號

格式化: 左右對齊

已刪除: sub-seasonal …ST variation is examined between…rom phase 1 and…o 8 averaged within the domain of …

已設定格式

已刪除: latent heat flux (

已刪除: represented by …reen shading), outgoing longwave radiation (…LR, represented by …(yellow bar chart), net surface solar radiation (…SNS, represented by …orange bar chart), 850-hPa zonal wind (…850, represented by …(purple bar chart), 30-m depth oceanic temperature (30-m … (multiplied by 100, represented by …lack line), and sea surface temperatures (…ST (multiplied by 10, represented

已設定格式

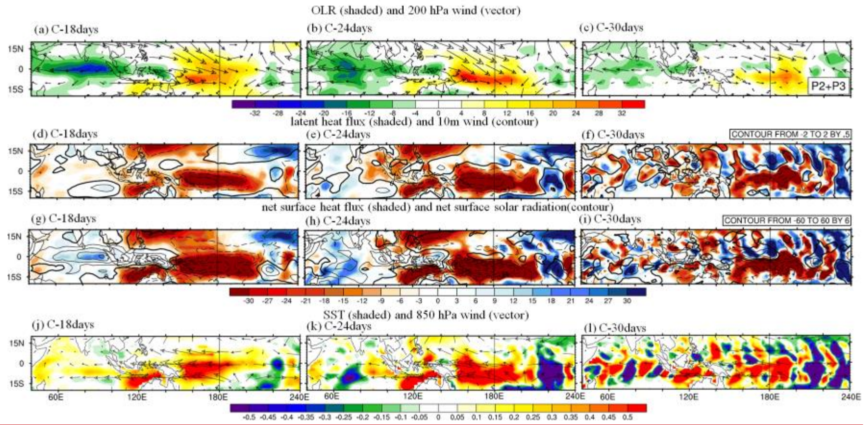

Figure 8. Averaged 20–100-day filtered fields at phase 2–3. (Upper row) OLR (W m^{-2}, shaded) and 200 hPa zonal and meridional wind anomaly (m s^{-1}, vector with reference vector shown at the top right corner, latent heat flux (W m^{-2}, shaded, positive representing upward), and 10-m wind anomaly (m s^{-1}, contour interval 0.5). (Second row) net surface heat flux (W m^{-2}, shaded) and net solar radiation (W m^{-2}, contour interval 6). (Third row) SST (K, shaded) and 850 hPa zonal and meridional wind anomaly (m s^{-1}, vector with reference vector shown at the top right corner. The number of days used to generate the composite is shown at the bottom right corner. (a), (d), (g) and (j) are from C–18days; (b), (e), (h) and (k) are from C–24days, and (c), (f), (i) and (l) are from C–30days, respectively. Solid, dashed, and thick-black lines represent positive, negative, and zero values, respectively.

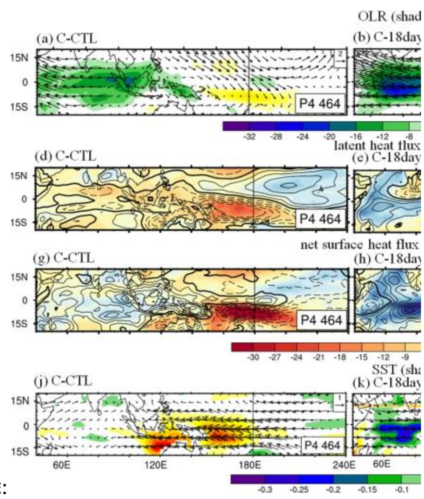

已刪除:

格式化: 左右對齊

已刪除: **10.** Phase 4 average

已刪除:)

已刪除: the

已刪除: (2 m s^{-1})

已刪除: of each panel at the top panel;

已刪除:) which

已刪除: anomaly represents

已刪除: ,

已刪除: 2); solid, dashed, and thick-black lines represent

已刪除: 3) at the third panel from the top, and

已刪除:)

已刪除: the

已刪除: (1 m s^{-1})

已刪除: of each panel at the bottom panel.

已刪除: of each panel and vertical black line of each panel

已刪除: CTL

已刪除: 18days

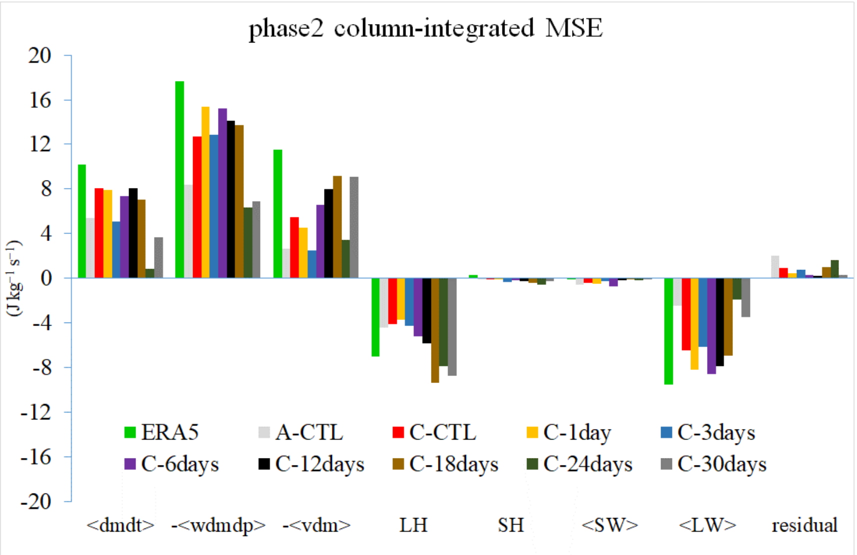

Figure 9. Averaged 20–100-day filtered column-integrated MSE budget terms ($J\ kg^{-1}\ s^{-1}$) in 10° S–0° N/S, 120–150° E for ERA5 and all model simulations. Colors represent different datasets: green for REA5, light gray for A–CTL, red, orange and wathet blue for high-frequency experiments (C–CTL, C–1day, and C–3days, respectively), purple, black, dark brown, dark green, and dark gray for low-frequency experiments (C–6days, C–12days, C–18days, C–24days, and C–30days, respectively). The bars from left to right represent MSE tendency (<dmdt>), vertical MSE advection (-<wdmdp>), horizontal MSE advection (-<vdm>), surface latent heat flux (LH), surface sensible heat flux (SH), shortwave radiation flux (<SW>), longwave radiation flux (<LW>), and residual terms.

已刪除: 分頁符號

格式化: 左右對齊

已刪除: across the domain (10

已刪除:)…for REA5

已設定格式

已設定格式

已刪除: Different colors

已設定格式: 預設段落字型, 字型色彩: 自動

已刪除:),… respectively,

已設定格式: 預設段落字型, 字型色彩: 自動

已刪除: blue…lack, dark brown, dark green, and dark gray

已設定格式

已刪除: fluxes

已設定格式

已刪除: fluxes

已設定格式

已刪除: fluxes

已設定格式

已刪除: fluxes

已設定格式

已刪除: >)

已設定格式

已刪除: , respectively

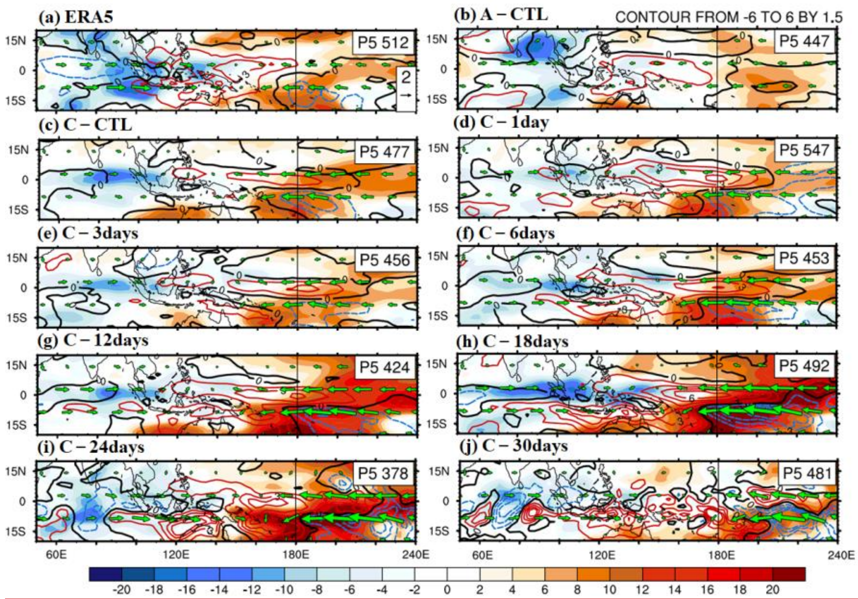

Figure 10. Filtered the column-integrated MSE tendency (J kg−1 s−1, shading), precipitation (mm d−1, contours interval 1.5) and 850-hPa wind (green vector, reference vector 2 m s−1) in phase 5: (a) ERA5, (b) A−CTL, (c) C−CTL, (d) C−1day, (e) C−3days, (f) C−6days, (g) C−12days, (h) C−18days, (i) C−24days, and (i) C−30days. Solid-red, dashed-blue, and thick-black curves represent positive, negative, and zero values, respectively.

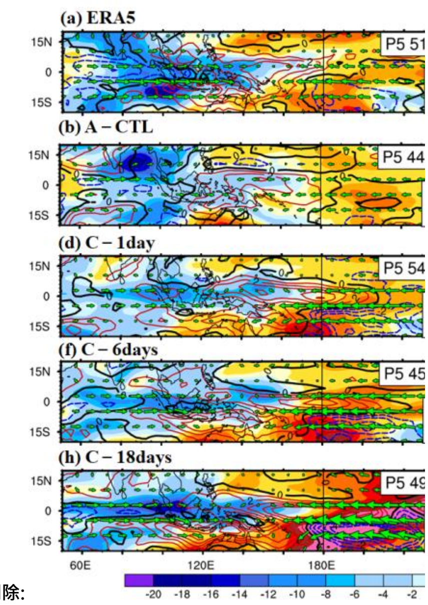

已刪除:

已刪除: **12.** Phase 5 anomalies of 20–100-day filtered

已設定格式: 非上標/ 下標

已設定格式: 非上標/ 下標

格式化: 左右對齊

已設定格式: 非上標/ 下標

已刪除: 0

已刪除:) with the

已設定格式: 非加寬 / 緊縮

已刪除: (

已設定格式: 非加寬 / 緊縮

已設定格式: 非上標/ 下標

已設定格式: 非上標/ 下標, 非加寬 / 緊縮

已設定格式: 非加寬 / 緊縮

已刪除: based on

已刪除: and

已刪除: The solid

已刪除: The vertical black line in each panel indicates the dateline.

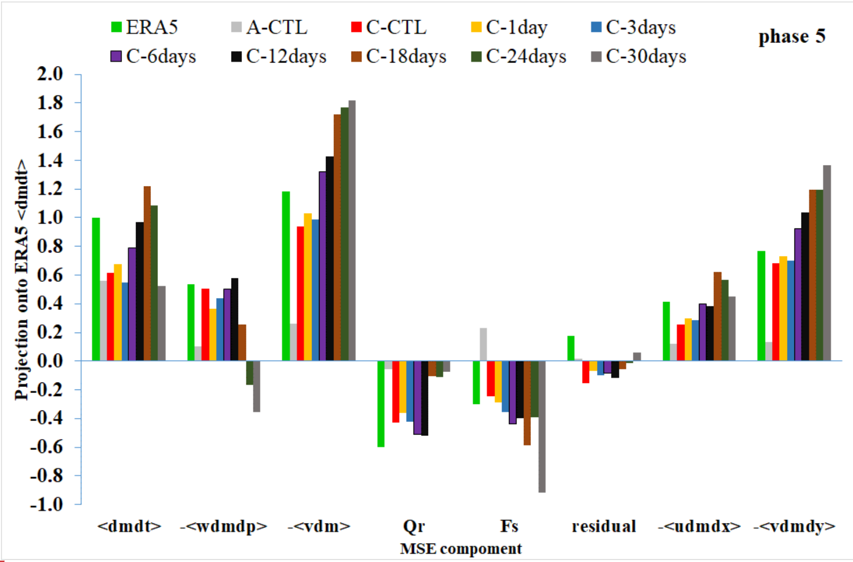

Figure 11. The projection of each MSE component onto the ERA5 column-integrated MSE tendency at phase 5 over the MC (20° S–20° N, 90–210° E): <dmdt>, -<wdmdp>, -<vdm>, Qr, Fs, and residual; decomposition of horizontal MSE advection to zonal and meridional advection (-<udmdt> and -<vdmdy>).

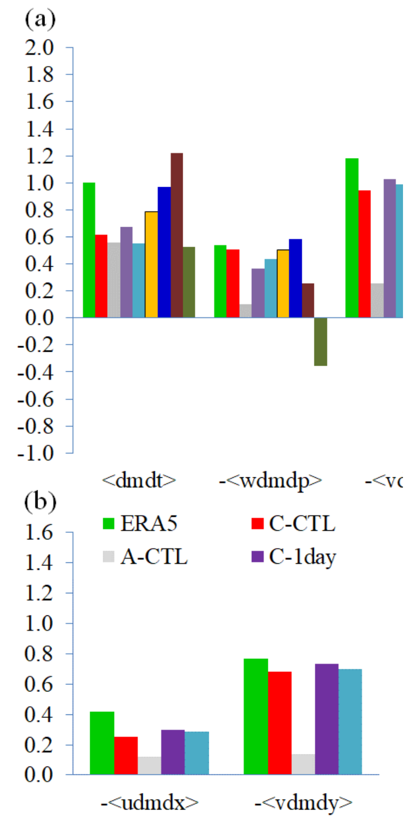

已刪除:

已刪除: **13.** (a)

已設定格式: 字型: 粗體

已刪除: relative role…rojection of each MSE component of …nto the ERA5 column-integrated MSE tendency at phase 5 through the projection of the spatial pattern of each MSE budget …

格式化: 左右對齊

已設定格式

已刪除:) onto the total MSE tendency pattern (Fig. 12a). (b–c) Decomposite of the total

已刪除: based on…o zonal and meridional components of high-frequency SST feedback experiments (C–CTL, A–CTL, C–1day and C–3days)…dvection (-<udmdt> and low-

已設定格式: 字型: Times New Roman

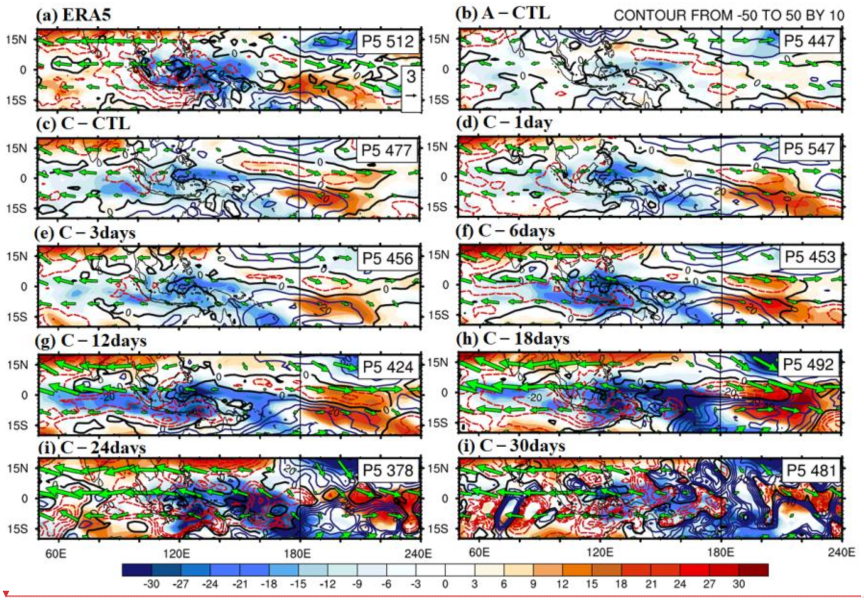

Figure 12. Filtered column-integrated vertical (J kg−1 s−1, shading) and horizontal MSE advection (J kg−1 s−1, contours interval 6.0), and 200-hPa wind (green vector with reference vector 3 m s−1): (a) ERA5, (b) A−CTL, (c) C−CTL, (d) C−1day, (e) C−3days, (f) C−6days, (g) C−12days, (h) C−18days, (i) C−24days, and (j) C−30days. Solid-blue, dashed-red, and thick-black curves represent positive, negative, and zero values, respectively.

已刪除:

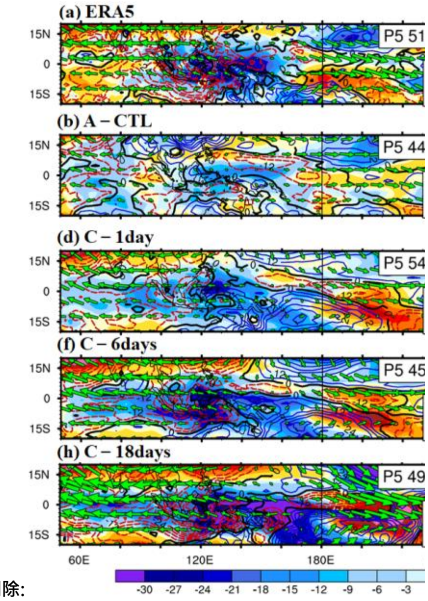

已刪除: **14.** Phase 5 anomalies of 20–100-day filtered the

已刪除: MSE advection

已設定格式

格式化: 左右對齊

已刪除:), column-integrated

已刪除:)…, and 200-hPa wind (green vector)

已設定格式

已設定格式: 非加寬 / 緊縮

已刪除: the

已設定格式: 非加寬 / 緊縮

已刪除: (

已設定格式

已刪除:) based on…: (a) ERA5, (b) A−CTL, (c) C−CTL, (d) C−1day, (e) C−3days, (f) C−6days, (g) C−12days, (h) C−18days, (i) C−24days, and (i…) C−30days. The solid…olid-blue, dashed-red, and thick-black curves represent positive, negative, and zero values, respectively. The vertical black line in each panel indicates the dateline.

分頁符號

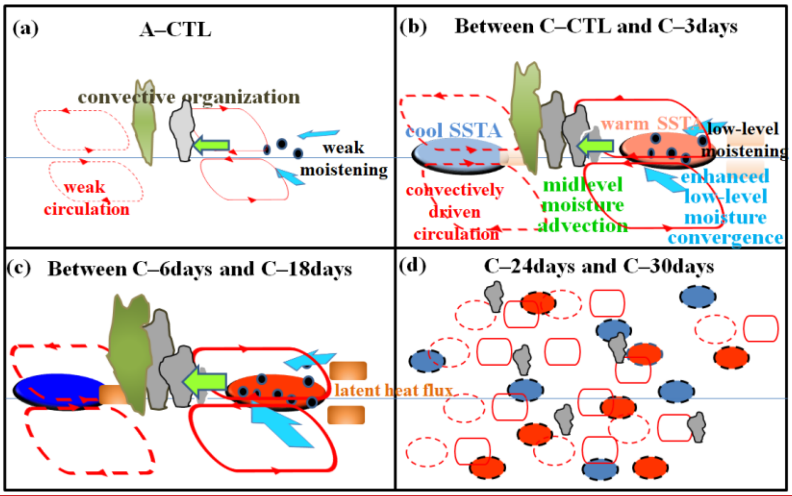

Figure 13. Schematic diagrams illustrate the anomalous circulation and moistening processes during the eastward propagation of the MJO in experiments: (a) A−CTL, (b) high-frequency SST feedback experiments (C−CTL, C−1day, and C−3days), (c) low-frequency SST feedback experiments (C−6days, C−12days, and C−18days), and (d) C−24days and C−30days experiment. In each panel, the horizontal line represents the equator. The size of clustering gray clouds indicates the strength of convective organization. A red ellipse indicates convection-driven circulation. In the coupled simulations, light red (blue) filled ovals represent warm (cold) SST anomalies, respectively, and grass green filled rectangle represent latent heat flux. Unresolved convective processes are indicated by black dots representing low-level moisture convergence. Low-level moisture convergence into the equatorial trough is shown by light blue arrows, while midlevel moisture advection is represented by left-pointing green arrows. The deeper colors or thicker lines on the map indicate stronger anomalies of the MJO perturbations. Note: The concept of the figure is based on DeMott et al. (2014).

已刪除:
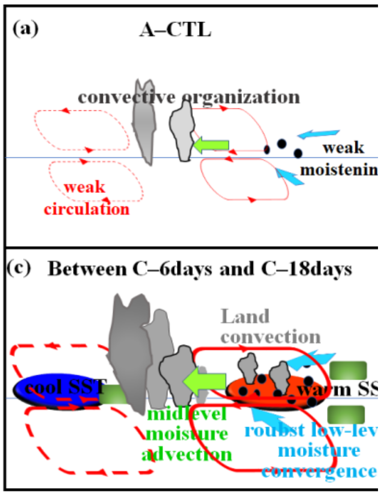

已刪除: **15.** The sketch map illustrates

格式化: 左右對齊

已刪除: equatorial

已刪除: anomalies

已刪除: boreal winter for various

已刪除: uncoupled

已刪除: of

已刪除: (size)

已刪除: conventionally

已刪除: anomalies

已刪除: a

已刪除: represents

已刪除: anomalies

已刪除: factors.

已刪除:), as depicted in Fig. 11.